Clarification of Nonadiabatic Chemical Dynamics by the Zhu-Nakamura Theory of Nonadiabatic Transition: From Tri-atomic Systems to Reactions in Solutions

Toshimasa Ishida[1], Shinkoh Nanbu[2] *, and Hiroki Nakamura[3] †

[1]Department of Chemistry, University of Malaya, 50603,
Kuala Lumpur, Malaysia.
e-mail: ishida@fukui.kyoto-u.ac.jp
[2]Department of Materials and Life Sciences,
Faculty of Science and Technology, Sophia University,
7-1 Kioi-cho, Chiyoda-ku, Tokyo, 102-8554, Japan.
e-mail: shinkoh.nanbu@sophia.ac.jp
[3]Institute for Molecular Science,
National Institutes of Natural Sciences,
Myodaiji, Okazaki 444-8585, Japan.
e-mail: nakamura@kba.biglobe.ne.jp

23/Feb./2017

Abstract

It is now confirmed that the Zhu-Nakamura (ZN) theory of nonadiabatic transition is useful to investigate various nonadiabatic chemical dynamics. The theory, being one-dimensional, presents a whole set of analytical formulas that enables us to treat the dynamics efficiently. It is also quite significant that classically forbidden transitions can be dealt with analytically. The theory can be combined with the trajectory surface hopping (TSH) method (ZN-TSH) and is demonstrated to be useful to clarify the dynamics of not only simple tri-atomic reactions but also large chemical systems. The whole set of analytical formulas directly applicable to practical systems is summarized

*Corresponding author. E-mail: shinkoh.nanbu@sophia.ac.jp
†Present address:Nakamura Institute of Chemical Dynamics, 3-10-20 Tatsumi Higashi, Okazaki, Japan

and the applications to polyatomic systems are illustrated. Examples of polyatomic molecules are H_2SO_4, NH_3, indolylmaleimide, cyclohexadiene (CHD), and retinal. The Fortran code for the whole set of Zhu-Nakamura formulas is provided in Appendix for the convenience of a reader who is interested in using them. The ZN-TSH method can be combined with the QM/MM method to clarify reaction dynamics in the surrounding environment. This is named as ZN-QM/MM-TSH. The particle-mesh Ewald (PME) method can also be combined with ZN-TSH to clarify reaction dynamics in solutions. This is named as ZN-PME-TSH. Formulations of these methods are presented together with practical applications. Examples treated by ZN-QM/MM-TSH are photoisomerization dynamics of retinal chromophore embedded in the protein environment. The differences in the isomerization mechanisms between rhodopsin and isorhodopsin are made clear. The faster and more efficient isomerization of rhodopsin compared to isorhodopsin is nicely reproduced. Examples of reactions in solutions are photoisomerizations of retinal and CHD. The experimentally observed long life time of the excited state of retinal is reproduced and is found to be due to the long-range solvation effect. The solvent dependent branching ratios of CHD:hexatriene(HT) are clarified for the ethanol and hexane solvents by the ZN-PME-TSH method. Both ZN-QM/MM-TSH and ZN-PME-TSH are thus demonstrated to be promising methods to deal with a wide range of nonadiabatic dynamics in large chemical and biological systems.

1. Introduction

It is well known now that a variety of chemical dynamic processes, for instance photo-chemical processes such as photo-isomerization, proceed through conical intersections (CI) of potential energy surfaces[1]. The transition at CI is nothing but nonadiabatic transition between adiabatic potential energy surfaces[2]. The significance of nonadiabatic chemical dynamics is well recognized and the field is expected to be further developed[3]. For instance, various molecular functions such as photochromism[4], molecular switch[2, 5] and molecular machine[6, 7] may be controlled by the nonadiabatic transition. The concept of "nonadiabatic transition" is actually very general and plays crucial roles not only in chemistry but also in physics, biology and other fields[2]. Examples are nuclear reactions[8, 9], surface physics [10], solid state physics[11], tunnel junctions[12, 13, 14], quantum dots [15, 16, 17, 18], solar cell[19], neutrino conversion [20, 21], photosynthesis[22, 23] and various biological processes[24, 25].

Because of the importance of the transition, there have been developed many analytical theories [2, 26, 27, 28, 29] since the pioneering works done by Landau[30], Zener[31] and Stückelberg[32]. There are time-dependent and time-independent versions in which the latter one is more difficult to formulate and relevant to chemical processes[2]. Zhu and Nakamura formulated a theory (ZN theory) which provides a whole set of analytical formulas not only for the transition probabilities but also for

the phases induced by the transition[2, 33]. There are two types of potential curve crossings: one is Landau-Zener type (see Fig.1) in which two diabatic potentials cross with the same sign of slopes and the other is nonadiabatic tunnel type (see Fig.2) in which two diabatic potentials cross with opposite signs of slopes and a potential barrier is created. The ZN theory not only largely improves the famous Landau-Zener formula in the classically allowed region (energy $\geq$ crossing energy), but also provides the analytical formulas for the classically forbidden transitions, covering the whole range of energy. It should be noted that the classically forbidden transitions are not negligible at all. The whole expressions can be evaluated with use of the knowledge of adiabatic potentials and no diabatization is needed. This is very convenient, because quantum chemical *ab initio* computations provide adiabatic potentials uniquely and diabatization procedure cannot be unique.

Since real chemical processes proceed, naturally, in a multi-dimensional space of nuclear coordinates, the classical or the semiclassical mechanics is usually employed to describe nuclear motions, while quantum mechanical, i.e., quantum chemical, methods are used for electronic structure computations. The full quantum mechanical treatment such as the wave packet propagation method or multi-channel time-dependent Hartree (MCTDH) method has been devised and successfully applied to various processes[34], but it would be a formidable task for real high dimensional chemical and biological systems, including accurate *ab initio* computations of global potential energy surfaces. The idea of surface hopping based on classical trajectories of nuclear motion is usually employed[35, 36]. The fewest switches surface hopping (FSSH) method proposed by Tully[37] has been widely used with various modifications[38, 39, 40, 41]. Basically, the time-dependent coupled equations are solved numerically along classical trajectories with the nonadiabatic coupling employed as the cause of the nonadiabatic transition. The ZN theory can be combined with this idea of surface hopping. The nonadiabatic transition is assumed to occur at the avoided crossing of adiabatic potential energy curves in the direction of nonadiabatic coupling vector and thus the decoherence problem[41] does not arise. Besides, classically forbidden transitions can be treated, as mentioned above, which is not possible by other available semiclassical methods based on classical trajectories. The quantum chemical *ab initio* computations of potential energy surfaces of high quality can be carried out on-the-fly. Furthermore, the method can be combined with the QM/MM method or the particle-mesh Ewald summation method to treat large scale systems such as photo-isomerization of retinal in protein environment and reactions in solutions.

This review article is organized as follows: the next section summarizes the whole set of ZN formulas directly applicable to practical systems. One numerical example is presented for one-dimensional model potentials to demonstrate how the theory works well even for classically forbidden transitions. The Fortran code for the formulas is provided in Appendix for the convenience of the reader who is interested in applying the ZN formulas. In Section 3 various methods to treat chemical dynamics with use of the ZN formulas are explained. The first one is the Zhu-Nakamura

trajectory surface hopping (ZN-TSH) method by which the over-all reaction probability is calculated from the ratio between the number of reactive trajectories and the total number of trajectories. The effects of phases are not taken into account in this treatment. The second one is the Herman-Kluk type semiclassical initial value representation method[42, 43, 44] with use of the ZN formulas (ZN-HKSCIVR), in which the phases are incorporated. This is appropriate for evaluating transition probability *amplitude* and absorption spectrum. In the third subsection a method to evaluate reaction rate constant of nonadiabatic dynamics is presented. Especially, the simple rate constant expression that improves the famous Marcus formula for electron transfer is provided. The last subsection describes how to treat the effects of environment. Namely, the combinations of the ZN theory with QM/MM and particle-mesh Ewald summation methods are discussed. In Section 4 numerical applications of the above mentioned methods are presented for various practical processes such as chemical reactions and absorption spectrum in tri- and tetra-atomic systems, reaction rate constant of electron transfer, photochemical dynamics of polyatomic molecules, photo-isomerization of retinal in vacuo and in protein environment and reactions in solutions. Section 5 concludes the paper by discussing future perspectives of the field of nonadiabatic chemical dynamics. Semiclassical molecular dynamics (MD) simulation method can be developed by taking into account not only nonadiabatic transitions but also quantum mechanical tunneling effects[45].

2. Zhu-Nakamura formulas[2]

A whole set of formulas of the Zhu–Nakamura theory are summarized here. It should be noted that the theory has the following nice features and can be easily utilized for various applications:
(1) All the probabilities are expressed in simple analytical forms.
(2) All the phases induced by nonadiabatic transitions are provided in compact analytical forms.
(3) All the basic parameters can be directly estimated from adiabatic potentials on the real axis.
This means that (i) no non-unique diabatization procedure is needed, (ii) no complex calculus is necessary, (iii) no nonadiabatic coupling information is required, and (iv) the theory works for whole range of energy and coupling strength.
The formulas presented here contain some empirical corrections so that they can cover practically the whole range of parameters a^2 and b^2 (see below). Some complex integrals up to the complex crossing point are simplified. These are explained in each relevant section.

When the diabatic potentials are available, the two basic dimensionless parameters $a^2(\geq 0)$ and $b^2(-\infty < b^2 < \infty)$ are defined by

$$a^2 = \frac{\hbar^2}{2\mu} \frac{F(F_1 - F_2)}{8V_X^3}$$

(2. 1)

4

and

$$b^2 = (E - E_X)\frac{F_1 - F_2}{2FV_X}, \qquad (2.\ 2)$$

where μ is the mass, F_j $(j = 1, 2)$ is the slope of the $j-$th diabatic potential with $F = \sqrt{|F_1 F_2|}$, V_X is the diabatic coupling and E_X is the energy at the avoided crossing point (see Eq.(2. 6)). Without loss of generality $F_1 - F_2$ is assumed to be positive. These parameters effectively represent the coupling strength and energy: $a^2 \gg 1, a^2 \sim 1$ and $a^2 \ll 1$ correspond to weak, intermediate, and strong coupling regime, respectively.

As mentioned above, there are two types of crossings: Landau-Zener type and nonadiabatic tunneling type.
(A) Landau-Zener case (see Fig.1)
In terms of adiabatic potentials $E_j(R)(j = 1, 2)$ these parameters a^2 and b^2 can be estimated directly from them as

$$a^2 = \sqrt{d^2 - 1}\frac{\hbar^2}{\mu(T_2^{(0)} - T_1^{(0)})^2(E_2(R_0) - E_1(R_0))}, \qquad (2.\ 3)$$

$$b^2 = \sqrt{d^2 - 1}\frac{E - (E_2(R_0) + E_1(R_0))/2}{(E_2(R_0) - E_1(R_0))/2}, \qquad (2.\ 4)$$

where

$$d^2 = \frac{[E_2(T_1^{(0)}) - E_1(T_1^{(0)})][E_2(T_2^{(0)}) - E_1(T_2^{(0)})]}{[E_2(R_0) - E_1(R_0)]^2}, \qquad (2.\ 5)$$

where the position R_0 is defined as the minimum separation of the two adiabatic potentials and E_X is defined by

$$E_X = [E_1(R_0) + E_2(R_0)]/2 = E_1(T_1^0) = E_2(T_2^0). \qquad (2.\ 6)$$

It should be noted that even when the diabatic potentials are available, it is better to use above expressions defined in terms of adiabatic potentials, since it is confirmed that they are more accurate.
(B) Nonadiabatic tunneling case (see Fig.2)
The parameters a^2 and b^2 originally defined by Eqs.(2. 1) and (2. 2) can be used when diabatic potentials are available; but these can also be estimated directly from adiabatic potentials by

$$a^2 = \frac{(1 - \gamma^2)\hbar^2}{\mu(R_b - R_t)^2(E_b - E_t)} \qquad (2.\ 7)$$

and

$$b^2 = \frac{E - (E_b + E_t)/2}{(E_b - E_t)/2}, \qquad (2.\ 8)$$
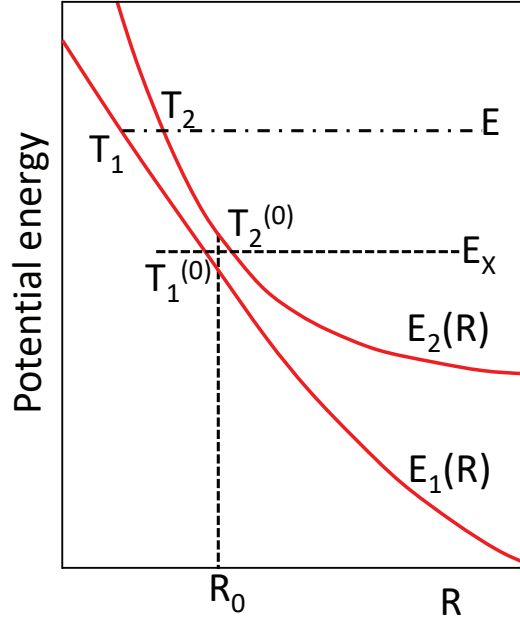
5

Figure 1: Landau-Zener type potential curve crossing.

where $E_b(E_t)$ is the bottom (top) of the upper (lower) adiabatic potential and

$$\gamma = \frac{E_b - E_t}{E_2([R_b + R_t]/2) - E_1([R_b + R_t]/2)}. \tag{2.9}$$

When $R_b = R_t$, $\gamma = 1$ and

$$a^2 = \frac{\hbar^2}{4\mu(E_b - E_t)} \left[\frac{\partial^2 E_2(R)}{\partial R^2} \bigg|_{R=R_b} - \frac{\partial^2 E_1(R)}{\partial R^2} \bigg|_{R=R_t} \right]. \tag{2.10}$$

2.1. Classically allowed transition

2.1.1. Landau-Zener case $(E \geq E_2(R_0))$(see Fig.1)

The nonadiabatic transition probability for one passage of the crossing point is given by

$$p_{ZN} = \exp\left[-\frac{\pi}{4a|b|} \left(\frac{2}{1 + \sqrt{1 + b^{-4}(0.4a^2 + 0.7)}} \right)^{1/2} \right]. \tag{2.11}$$

It should be noted that the Landau-Zener formula is simply given by
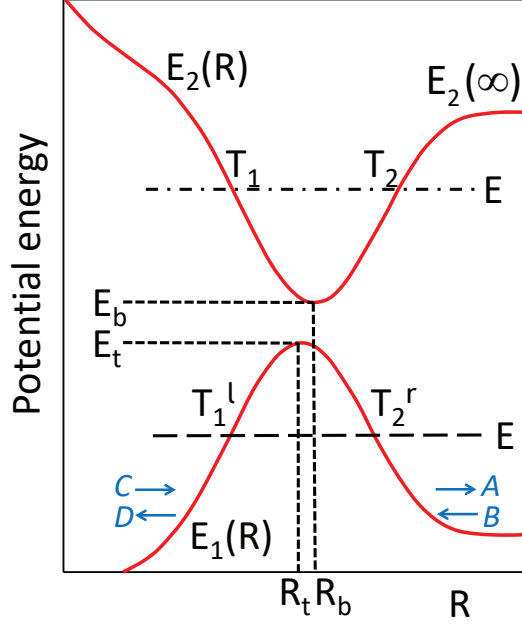
$$p_{LZ} = \exp[-\frac{\pi}{4a|b|}], \tag{2.12}$$

Figure 2: Nonadiabatic-Tunneling type potential curve crossing.

which goes to zero as $|b| \to 0$. The factor $0.4a^2 + 0.7$ is originally unity and is confirmed to be slightly better than unity (see (a) of [33]).

When the phases induced by nonadiabatic transition are needed, the following transition matrix I_X at the avoided crossing point R_0 should be used:

$$\begin{pmatrix} C \\ D \end{pmatrix} = I_X \begin{pmatrix} A \\ B \end{pmatrix}, \tag{2. 13}$$

where A and B (C and D) are the coefficients of the wave functions at $R = R_0 + 0$ ($R = R_0 - 0$). This matrix gives the transition amplitude at the crossing point and explicitly defined as

$$I_X = \begin{pmatrix} \sqrt{1 - p_{ZN}}\, e^{i(\psi_{ZN} - \sigma_{ZN})} & -\sqrt{p_{ZN}}\, e^{i\sigma_0^{ZN}} \\ \sqrt{p_{ZN}}\, e^{-i\sigma_0^{ZN}} & \sqrt{1 - p_{ZN}}\, e^{-i(\psi_{ZN} - \sigma_{ZN})} \end{pmatrix}, \tag{2. 14}$$

where

$$\psi_{ZN} = \sigma_{ZN} + \phi_S \tag{2. 15}$$

with

$$\phi_S = -\frac{\delta_\psi}{\pi} + \frac{\delta_\psi}{\pi} \ln\left(\frac{\delta_\psi}{\pi}\right) - \arg \Gamma\left(i\frac{\delta_\psi}{\pi}\right) - \frac{\pi}{4}. \tag{2. 16}$$

The various parameters are defined as follows:

$$\delta_\psi = \delta_{ZN}\left(1 + \frac{5a^{1/2}}{a^{1/2} + 0.8}10^{-\sigma_{ZN}}\right) \tag{2. 17}$$

7

and

$$\sigma_0^{\text{ZN}} + i\delta_0^{\text{ZN}} \equiv \int_{R_0}^{R_*} [K_1(R) - K_2(R)]dR \simeq \frac{\sqrt{2}\pi}{4a} \frac{F_-^C + iF_+^C}{F_+^2 + F_-^2}, \qquad (2.\ 18)$$

where the final approximate expression is derived by using the linear potential model and 3-point quadrature (see (i) of [33]),

$$K_j(R) = \sqrt{\frac{2\mu}{\hbar^2}(E - E_j(R))}, \qquad (2.\ 19)$$

$$
\begin{aligned}
F_\pm &= \sqrt{\sqrt{(b^2 + \gamma_1)^2 + \gamma_2} \pm (b^2 + \gamma_1)} \\
&\quad + \sqrt{\sqrt{(b^2 - \gamma_1)^2 + \gamma_2} \pm (b^2 - \gamma_1)},
\end{aligned}
\qquad (2.\ 20)
$$

$$F_+^C = F_+ \left(b^2 \longrightarrow \left[b^2 - \frac{0.16b_x}{\sqrt{b^4 + 1}} \right] \right), \qquad (2.\ 21)$$

$$F_-^C = F_- \left(\gamma_2 \longrightarrow \frac{0.45\sqrt{d^2}}{1 + 1.5e^{2.2b_x|b_x|^{0.57}}} \right) \qquad (2.\ 22)$$

and

$$b_x = b^2 - 0.9553, \qquad \gamma_1 = 0.9\sqrt{d^2 - 1}, \qquad \gamma_2 = 7\sqrt{d^2}/16. \qquad (2.\ 23)$$

The parameters σ_{ZN} and δ_{ZN} are given as follows:

$$\sigma_{\text{ZN}} = \int_{T_1}^{R_0} K_1(R)dR - \int_{T_2}^{R_0} K_2(R)dR + \sigma_0^{\text{ZN}} \qquad (2.\ 24)$$

and

$$\delta_{\text{ZN}} = \delta_0^{\text{ZN}}. \qquad (2.\ 25)$$

The correction factor in Eq.(2. 17) is introduced empirically (see (c) of [33]).

2.1.2. Nonadiabatic tunneling case $(E \geq E_b)$ (see Fig.2)

The transition probability for one passage of the crossing point is given as

$$p_{\text{ZN}} = \exp\left[-\frac{\pi}{4ab} \left(\frac{2}{1 + \sqrt{1 - b^{-4}(0.72 - 0.62a^{1.43})}} \right)^{1/2} \right]. \qquad (2.\ 26)$$

The factor $0.72 - 0.6a^{1.43}$ is originally unity and is confirmed to be slightly better than unity (see (b) of [33]). When $E \leq E_2(\infty)$, the overall transmission probability from left to right or vice versa is the physically meaningful quantity and is given by

$$P_{12} = \frac{4\cos^2(\sigma_{\text{ZN}} - \bar{\phi}_{\text{S}})}{4\cos^2(\sigma_{\text{ZN}} - \bar{\phi}_{\text{S}}) + (p_{\text{ZN}})^2/(1 - p_{\text{ZN}})}, \qquad (2.\ 27)$$

where

$$\sigma_{ZN} = \int_{T_1}^{T_2} K_2(R)dR \tag{2. 28}$$

with $K_2(R)$ defined by Eq.(2. 19),

$$\bar{\phi}_S = \phi_S + h_1, \tag{2. 29}$$

$$h_1 = \frac{0.23a^{1/2}}{a^{1/2} + 0.75}40^{-\sigma_{ZN}}, \tag{2. 30}$$

$$\phi_S = -\frac{\delta_{ZN}}{\pi} + \frac{\delta_{ZN}}{\pi}\ln(\frac{\delta_{ZN}}{\pi}) - \arg\Gamma(i\frac{\delta_{ZN}}{\pi}) - \frac{\pi}{4}, \tag{2. 31}$$

$$\delta_{ZN} = \frac{\pi}{16ab}\frac{\sqrt{6 + 10\sqrt{1 - b^{-4}}}}{1 + \sqrt{1 - b^{-4}}}. \tag{2. 32}$$

The correction factor h_1 is introduced empirically (see (c) of [33]). The expression of δ_{ZN} is derived by using the linear potential model (see (d) of [33]). It should be noted that when $\psi_{ZN} \equiv \sigma_{ZN} - \bar{\phi}_S = (n + 1/2)\pi(n = 0, 1, 2, , , ,)$, P_{12} becomes zero. Namely, the intriguing phenomenon of complete reflection occurs, when this condition is satisfied.

When the phases are needed, the transition matrix I_X at $E \geq E_b$ defined below should be used,

$$I_X = \begin{pmatrix} \sqrt{1 - p_{ZN}}e^{i\phi_S} & \sqrt{p_{ZN}}e^{i\sigma_0^{ZN}} \\ -\sqrt{p_{ZN}}e^{-i\sigma_0^{ZN}} & \sqrt{1 - p_{ZN}}e^{-i\phi_S} \end{pmatrix}, \tag{2. 33}$$

where ϕ_S is the same as Eq.(2. 31). At $E > E_2(\infty)$, this I_X is used in the same way as I_X in the Landau-Zener case. When the trapping by the upper adiabatic potential occurs ($E \leq E_2(\infty)$), we have to use the following reduced scattering matrix (S^R) that describes the overall transmission/reflection amplitudes from the entrance to the exit:

$$S^R = \frac{1}{1 + U_1 U_2}\begin{pmatrix} e^{i\Delta_{11}} & U_2 e^{i\Delta_{12}} \\ U_2 e^{i\Delta_{12}} & e^{i\Delta_{22}} \end{pmatrix} \tag{2. 34}$$

with

$$U_2 = 2i\,\text{Im}(U_1)/(|U_1|^2 - 1), \tag{2. 35}$$

where

$$\Delta_{12} = \sigma_{ZN}, \tag{2. 36}$$

$$\Delta_{11} = 2\int_{T_1}^{R_b} K_2(R)dR - 2\sigma_0^{ZN}, \tag{2. 37}$$

$$\Delta_{22} = 2\int_{R_b}^{T_2} K_2(R)dR + 2\sigma_0^{ZN}, \tag{2. 38}$$

$$\sigma_0^{ZN} = \left(\frac{R_b - R_t}{2}\right)\left\{K_1(R_t) + K_2(R_b) + \frac{1}{3}\frac{[K_1(R_t) - K_2(R_b)]^2}{K_1(R_t) + K_2(R_b)}\right\}, \tag{2. 39}$$

$$U_1 = i\sqrt{1 - p_{ZN}}\exp[i(\sigma_{ZN} - \bar{\phi}_S)] \tag{2. 40}$$

and σ_{ZN} [ϕ_S] is given by Eq.(2. 28) [Eq.(2. 31)]. The index of the S^R-matrix corresponds to left or right side of the barrier.

9

2.2. Classically forbidden transition

2.2.1. Landau-Zener case $(E \leq E_2(R_0))$ (see Fig.1)

The overall transition probability from the state 1 to state 2 is given by

$$P_{12} = 4p_{ZN}(1 - p_{ZN})\sin^2(\phi_S + \sigma_0^{ZN}), \qquad (2.\ 41)$$

where

$$p_{ZN} = [1 + B(\sigma_{ZN}/\pi)\exp(2\delta_{ZN}) - g_1\sin^2(\sigma_{ZN})]^{-1}, \qquad (2.\ 42)$$

ϕ_S and σ_0^{ZN} are given by Eq.(2. 16) and Eq.(2. 18),

$$B(x) = \frac{2\pi x^{2x}e^{-2x}}{x\Gamma^2(x)} \qquad (2.\ 43)$$

and

$$g_1 = \frac{3\sigma_{ZN}}{\pi\delta_{ZN}}\ln(1.2 + a^2) - \frac{1}{a^2}. \qquad (2.\ 44)$$

The parameters σ_{ZN} and δ_{ZN} are given below (Eq.(2. 50)-Eq.(2. 53)).

When the phases induced by the transition are needed, the reduced scattering matrix (S^R) which provides the transition amplitude from the turning point on the entrance adiabatic surface to that on the exit adiabatic surface should be used:

$$S^R = I_X^T \cdot I_X, \qquad (2.\ 45)$$

where the superscript T means "transpose" and the transition matrix I_X is formally given by Eq.(2. 14) with the parameters ψ_{ZN} and σ_0^{ZN} replaced by the following expressions:

$$\psi_{ZN} = \arg(U), \qquad (2.\ 46)$$

where

$$\text{Re } U = \cos(\sigma_{ZN})\left\{\sqrt{B(\sigma_{ZN}/\pi)}e^{\delta_{ZN}} - g_2\sin^2(\sigma_{ZN})\frac{e^{-\delta_{ZN}}}{\sqrt{B(\sigma_{ZN}/\pi)}}\right\}, \qquad (2.\ 47)$$

$$\text{Im } U = \sin(\sigma_{ZN})\left\{B(\sigma_{ZN}/\pi)e^{2\delta_{ZN}} - g_2^2\sin^2(\sigma_{ZN})\cos^2(\sigma_{ZN})\frac{e^{-2\delta_{ZN}}}{B(\sigma_{ZN}/\pi)}\right.$$
$$\left. + 2g_1\cos^2(\sigma_{ZN}) - g_2\right\}^{1/2} \qquad (2.\ 48)$$

with σ_0^{ZN} is given by Eq.(2. 18) and

$$g_2 = 1.8(a^2)^{0.23}e^{-\delta_{ZN}}. \qquad (2.\ 49)$$

The factors g_1 and g_2 are originally unity. The first (second) factor of g_1 is responsible for $a^2 \gg 1 (a^2 \ll 1)$ (see (a) of [33]). The parameters σ_{ZN} and δ_{ZN} are given as follows:
(1) At $E_2(R_0) > E > E_1(R_0)$,

$$\sigma_{ZN} = \int_{T_1}^{R_0} K_1(R)dR + \sigma_0^{ZN} \tag{2.50}$$

and

$$\delta_{ZN} = \int_{R_0}^{T_2} K_2(R)dR + \delta_0^{ZN}. \tag{2.51}$$

(2) At $E \leq E_1(R_0)$,

$$\sigma_{ZN} = \sigma_0^{ZN} \tag{2.52}$$

and

$$\delta_{ZN} = -\int_{R_0}^{T_1} |K_1(R)|dR + \int_{R_0}^{T_2} |K_2(R)|dR + \delta_0^{ZN}. \tag{2.53}$$

2.2.2. Nonadiabatic tunneling case

First, the overall transmission probability (P_{12}) from left to right or vice versa is the physically meaningful probability.
(1) At $E_b \geq E \geq E_t$

$$P_{12} = \frac{W^2}{1 + W^2}, \tag{2.54}$$

where

$$W = \frac{h_2}{a^{2/3}} \int_0^\infty \cos\left[\frac{t^3}{3} - \frac{b^2}{a^{2/3}}t - \frac{h_3}{a^{2/3}}\frac{t}{h_4 + a^{1/3}t}\right] dt, \tag{2.55}$$

$$h_2 = 1 + \frac{0.38}{a^2}(1 + b^2)^{1.2 - 0.4b^2}, \tag{2.56}$$

$$h_3 = \frac{\sqrt{a^2 - 3b^2}}{\sqrt{a^2 + 3}}\sqrt{1.23 + b^2} \tag{2.57}$$

and

$$h_4 = 0.61\sqrt{2 + b^2}. \tag{2.58}$$

The factors h_2, h_3 and h_4 are originally $1/2$, 1, and 1, respectively, and are confirmed to cover the whole range of a^2 (see (c) of [33]).
(2) At $E \leq E_t$

$$P_{12} = \frac{B(\sigma_c/\pi)e^{-2\delta_{ZN}}}{[1 + (0.5\sqrt{a^2}/[\sqrt{a^2 + 1}])B(\sigma_c/\pi)e^{-2\delta_{ZN}}]^2 + B(\sigma_c/\pi)e^{-2\delta_{ZN}}} \tag{2.59}$$

with

$$\sigma_c = \sigma_{ZN}(1 - 0.32 \times 10^{-2/a^2}e^{-\delta_{ZN}}), \tag{2.60}$$

$$\delta_{ZN} = \int_{T_1^l}^{T_1^r} |K_1(R)|dR, \tag{2.61}$$

11

and

$$\sigma_{\rm ZN} = \frac{\pi}{8a|b|} \frac{1}{2} \frac{\sqrt{6 + 10\sqrt{1 - 1/b^4}}}{1 + \sqrt{1 - 1/b^4}}, \tag{2. 62}$$

where the function $B(x)$ is given by Eq.(2. 43). It should be noted that when $a^2 \to 0$, namely, the upper adiabatic potential goes away, we have

$$P_{12} = \frac{e^{-2\delta_{\rm ZN}}}{1 + e^{-2\delta_{\rm ZN}}}, \tag{2. 63}$$

which agrees with the ordinary single potential barrier penetration probability. The factor $0.32 \times 10^{-2/a^2}$ in Eq.(2. 60) is originally 0 and confirmed to be better (see (c) of [33]). The simplified expression of $\sigma_{\rm ZN}$ is derived by using the linear potential model (see (d) of [33]).

When the phases are needed, what we have to use is the reduced scattering matrix ($S^{\rm R}$) defined by Eq.(2. 34) with U_2 in terms of U_1 is given by Eq.(2. 35). The parameters $\Delta_{12}, \Delta_{11}, \Delta_{22}$ and U_1 are defined as follows:
(1) At $E_{\rm b} \geq E \geq E_{\rm t}$

$$\Delta_{12} = \sigma_{\rm ZN}, \qquad \Delta_{11} = \sigma_{\rm ZN} - 2\sigma_0^{\rm ZN} \quad {\rm and} \quad \Delta_{22} = \sigma_{\rm ZN} + 2\sigma_0^{\rm ZN}, \tag{2. 64}$$

$$\sigma_0^{\rm ZN} = -\frac{1}{3}(R_{\rm t} - R_{\rm b})K_1(R_{\rm t})(1 + b^2), \tag{2. 65}$$

$$U_1 = i[\sqrt{1 + W^2}e^{i\phi} - 1]/W, \tag{2. 66}$$

$$\phi = \sigma_{\rm ZN} + \arg\Gamma\left(\frac{1}{2} + i\frac{\delta_{\rm ZN}}{\pi}\right) - \frac{\delta_{\rm ZN}}{\pi}\ln\left(\frac{\delta_{\rm ZN}}{\pi}\right) + \frac{\delta_{\rm ZN}}{\pi} - h_5, \tag{2. 67}$$

$$h_5 = 0.34\frac{a^{0.7}(a^{0.7} + 0.35)}{a^{2.1} + 0.73}(0.42 + b^2)\left(2 + \frac{100b^2}{100 + a^2}\right)^{\frac{1}{4}}, \tag{2. 68}$$

$$\sigma_{\rm ZN} = -\frac{1}{\sqrt{a^2}}\left[0.057(1 + b^2)^{\frac{1}{4}} + \frac{1}{3}\right](1 - b^2)\sqrt{5 + 3b^2}, \tag{2. 69}$$

$$\delta_{\rm ZN} = \frac{1}{\sqrt{a^2}}\left[0.057(1 - b^2)^{\frac{1}{4}} + \frac{1}{3}\right](1 + b^2)\sqrt{5 - 3b^2}, \tag{2. 70}$$

The empirical corrections used for h_5, $\sigma_{\rm ZN}$ and $\delta_{\rm ZN}$ are introduced by using the linear potential model (see (c) of [33]).
(2) At $E \leq E_{\rm t}$

$$\Delta_{12} = \Delta_{11} = \Delta_{22} = -2\sigma_{\rm ZN}, \tag{2. 71}$$

$${\rm Re}\,U_1 = \sin(2\sigma_c)\left\{\frac{0.5\sqrt{a^2}}{1 + \sqrt{a^2}}\sqrt{B\left(\frac{\sigma_c}{\pi}\right)}e^{-\delta_{\rm ZN}} + \frac{e^{\delta_{\rm ZN}}}{\sqrt{B(\sigma_c/\pi)}}\right\}, \tag{2. 72}$$

$${\rm Im}\,U_1 = \cos(2\sigma_c)\sqrt{\frac{({\rm Re}\,U_1)^2}{\sin^2(2\sigma_c)} + \frac{1}{\cos^2(2\sigma_c)}} - \frac{1}{2\sin(\sigma_c)}\left|\frac{{\rm Re}\,U_1}{\cos(\sigma_c)}\right|, \tag{2. 73}$$

The parameters σ_c and δ_{ZN} are given by Eqs.(2. 60) and (2. 61), respectively. The factor $0.5\sqrt{a^2}/(1 + \sqrt{a^2})$ is originally 0.25 and confirmed to be better (see (c) of [33]).

2.3. Numerical example

One example is shown here (see (g) of [33]). The following 4-state problem defined in atomic units is employed.

$$
\begin{aligned}
V_1(R) &= 0.037\exp[-1.3(R - 3.25)] - 0.034, \\
V_2(R) &= 0.037\exp[-1.3(R - 3.25)] - 0.012, \\
V_3(R) &= 0.4057[1 - \exp[-0.344(R - 3)]]^2 - 0.03, \\
V_4(R) &= 0.4057[1 - \exp[-0.344(R - 3)]]^2.
\end{aligned}
\tag{2. 74}
$$

The couplings are given by

$$
V_{13}(R) = V_{14}(R) = V_{23}(R) = V_{24}(R) = \frac{2V_0}{1 + \exp(R - 3)}, \quad V_{12}(R) = V_{34}(R) = 0.
\tag{2. 75}
$$

This model system represents some states of O_2 (reduced mass $= 29377.3$ m_e) [46]. Fig.3 shows the potential curves in the case of $V_0 = 0.002$ E_h. Fig.4 indicates the
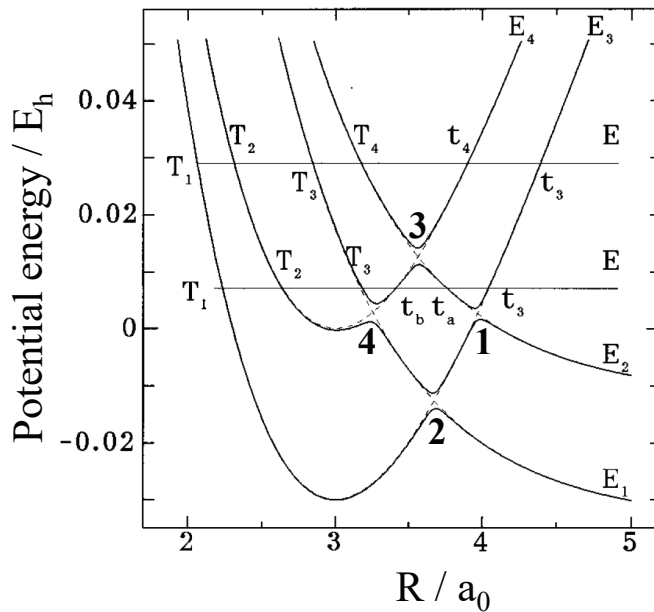

Figure 3: Four-state model potentials of Eq.(2. 74) with $V_0 = 0.002$ E_h. Reproduced from Ref.(g) in [33] by permission of American Institue of Physics (AIP).

transition probability from state 1 to 2 in the case of $V_0 = 0.004$ E_h in the energy
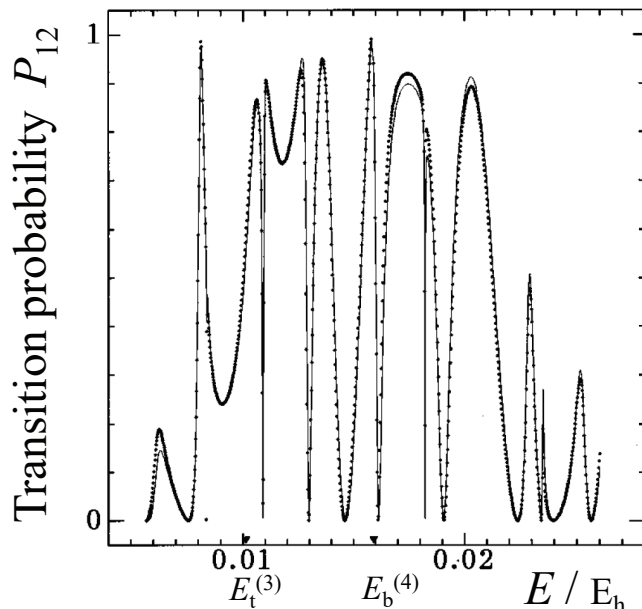
Figure 4: Transition probability vs. energy for the potential system of Fig.3 with $V_0 = 0.004$ E_h. $E_{top}^{(3)} = 0.01009$ E_h, $E_{bottom}^{(4)} = 0.0158$ E_h and the starting energy $E_{start} = 0.00568$ E_h. Reproduced from Ref.(g) in [33] by permission of AIP.

range covering the classically forbidden region of the avoided crossing between the highest and second highest adiabatic potentials. The parameters $a_j^2 (j = 1 - 4)$ corresponding to $V_0 = 0.004$ E_h are given as follows, where j represents the crossing position (see Fig.3):

$$(a_1^2, a_2^2, a_3^2, a_4^2) = (0.98, 0.55, 0.43, 0.24). \tag{2. 76}$$

It should be noted that the energy of the top (bottom) of the third (fourth) adiabatic potential is equal to

$$E_{top}^{(3)} = 0.01009 \text{ E}_h, \ E_{bottom}^{(4)} = 0.0158 \text{ E}_h \tag{2. 77}$$

and the starting energy of Fig.4 is 0.00568 E_h. It is clearly seen that the present semiclassical theory works very well, reproducing the detailed resonances. There are many more examples to demonstrate the accuracy of the theory[33].

3. How to treat dynamics

3.1. Zhu-Nakamura trajectory surface hopping (ZN-TSH) method

The ZN-TSH is the simplest method to estimate reaction probabilities by running classical trajectories on adiabatic potential energy surfaces. The probability is given

14

by the ratio of the number of relevant reactive trajectories to the total number of trajectories. As is well known, if the total number of trajectories is large enough, the ratio gives the proper estimate of the transition probability. The phases along trajectories are not taken into account in this method.

Nonadiabatic transitions in the vicinity of conical intersections are treated as follows: the adiabatic potential energy difference (ΔE) between the relevant surface and the nearest potential energy surface is computed along each classical trajectory and the minimum ΔE position is detected. That provides the position of transition. There the nonadiabatic coupling vector is evaluated and the direction of the vector provides the direction of transition. Two potential energy curves along this direction are used to evaluate the corresponding nonadiabatic transition probability by using the relevant Zhu-Nakamura formula. As was explained in the previous section, the necessary parameters can be estimated from the adiabatic potential curves. When the translational energy along the transition direction is larger than the energy at the avoided crossing point, the transition is the ordinary classically allowed one. The relevant transition probability is p_{ZN}. If the former energy turns out to be lower than the latter, the transition is classically forbidden and the corresponding Zhu-Nakamura probability P_{12} should be used. The judgment whether the transition is carried out or not is made by generating a random number p_{random}. There are two versions: one is ant-eater procedure and the other is ants procedure [47]. In the former case the transition is carried out when the Zhu-Nakamura probability is larger than p_{random} and in the latter case the trajectory is branched into two in which each trajectory is associated with the branching ratio given by the corresponding Zhu-Nakamura probability. Since the number of branched trajectories can be large in the ants procedure, the ant-eater procedure is simpler and is usually employed. When the transition is made, the kinetic energy along the transition direction changes because of the electronic energy difference ΔE and the appropriate modification of kinetic energy of the trajectory should be made. As can be understood in the above explanation, the nonadiabatic transition is considered only at the minimum energy separation and the nonadiabatic coupling vector is needed only to decide the transition direction there. Besides the transition probabilities can be estimated from the analytical formulas. Thus the method is much simpler than solving the time-dependent coupled differential equations with use of the nonadiabatic couplings all the way. It should be noted that the classically forbidden transitions cannot be properly treated by solving the time-dependent coupled equations based on classical trajectories.

If it is too much cpu-time consuming to compute nonadiabatic couplings, the following approximation can be employed[48]. In the vicinity of conical intersection we can assume the following diabatic Hamiltonian,

$$H = \begin{pmatrix} V_1 & V \\ V & V_2 \end{pmatrix} = \begin{pmatrix} \sum_j A_j x_j & \sum_j B_j x_j \\ \sum_j B_j x_j & -\sum_j A_j x_j \end{pmatrix}. \tag{3.1}$$

Then the nonadiabatic coupling vector $\vec{e} = \{e_j\}$ is equal to

$$
\begin{aligned}
e_j &= \frac{\frac{\partial V}{\partial x_j}(V_1 - V_2) - V\left(\frac{\partial V_1}{\partial x_j} - \frac{\partial V_2}{\partial x_j}\right)}{(\Delta E)^2} \\
&= \frac{\sum_k (A_k B_j - A_j B_k) x_k}{(\Delta E)^2},
\end{aligned}
\tag{3. 2}
$$

where
$$
\Delta E = \sqrt{\left(\sum_k A_k x_k\right)^2 + \left(\sum_k B_k x_k\right)^2}.
\tag{3. 3}
$$

On the other hand, the second derivative of ΔE is given by

$$
\frac{\partial^2 \Delta E}{\partial x_i \partial x_j} = \frac{-1}{(\Delta E)^3}\left[\left(\sum_k A_k x_k\right)^2 B_i B_j + \left(\sum_k B_k x_k\right)^2 A_i A_j - \left(\sum_k A_k x_k\right)\left(\sum_k B_k x_k\right)(A_i B_j + B_i A_j)\right].
\tag{3. 4}
$$

Thus, up to an irrelevant scale factor we have

$$
\frac{\partial^2 \Delta E}{\partial x_i \partial x_j} \propto e_i e_j.
\tag{3. 5}
$$

This gives a rank-1 matrix and the eigenvector of its only one non-zero eigenvalue provides the direction of the nonadiabatic coupling vector. This approximation works well, as will be demonstrated in Section 4.1.

3.2. Herman-Kluk type semiclassical initial value representation method with use of the Zhu-Nakamura formulas (ZN-HKSCIVR)

When coherence plays crucial roles in chemical dynamics, the transition *amplitude* should be evaluated with various phases taken into account. The best way to do this is to employ the initial value representation (IVR) devised by Miller[42]. This was combined with the idea of frozen Gaussian propagation approximation[43, 44]. Here we use this method.

The initial wave function $\psi(\mathbf{r}_0, t = 0)$ is expanded in terms of frozen Gaussian wave packets and the latter are propagated along classical trajectories. The total wave function at time t, $\psi(\mathbf{r}, t)$, is expressed as

$$
\psi(\mathbf{r}, t) = \int_{traj} \frac{d\mathbf{q}_0 d\mathbf{p}_0}{(2\pi)^N} g(\mathbf{r}; \mathbf{q}_t, \mathbf{p}_t) C_{\mathbf{q}_0, \mathbf{p}_0, t} \exp[i S_{\mathbf{q}_0, \mathbf{p}_0, t}] \int d\mathbf{r}_0 g^*(\mathbf{r}_0; \mathbf{q}_0, \mathbf{p}_0) \psi(\mathbf{r}_0, t = 0),
\tag{3. 6}
$$

where N is the dimensionality of configuration space, $S_{\mathbf{q}_0, \mathbf{p}_0, t}$ is the action integral along the classical trajectory propagated from $(\mathbf{q}_0, \mathbf{p}_0, t = 0)$ to $(\mathbf{q_t}, \mathbf{p_t}, t)$, and

$C_{\mathbf{q_0},\mathbf{p_0},t}$ is the Herman-Kluk pre-exponential factor along the trajectory. The frozen Gaussian wave packets $g(\mathbf{r};\mathbf{q},\mathbf{p})$ are defined by

$$g(\mathbf{r};\mathbf{q},\mathbf{p}) = (\frac{2\gamma}{\pi\hbar})^{N/4}\exp[-\gamma(\mathbf{r}-\mathbf{q})^2/\hbar + i\mathbf{p}\cdot(\mathbf{r}-\mathbf{q})/\hbar], \qquad (3.\ 7)$$

where γ is a constant parameter common to all the wave packets. The pre-exponential factor $C_{\mathbf{q},\mathbf{p},t}$ is defined by

$$C_{\mathbf{q},\mathbf{p},t} = \Big[\mathrm{Det}(\frac{\partial\mathbf{p}_t}{\partial\mathbf{p_0}} + \frac{\partial\mathbf{q}_t}{\partial\mathbf{q_0}} - 2i\gamma\frac{\partial\mathbf{q}_t}{\partial\mathbf{p_0}} + \frac{i}{2\gamma}\frac{\partial\mathbf{p}_t}{\partial\mathbf{q_0}})\Big]^{1/2}. \qquad (3.\ 8)$$

As is easily understood, the above formulation is for the dynamics on adiabatic potential energy surface. In order to treat nonadiabatic dynamics the corresponding transition amplitude from Zhu-Nakamura theory is incorporated into the above formulation. In the case of classically allowed transition from the state j to i, the amplitude I_{ij} from the transition matrix I_X should be incorporated (see Eqs.(2. 14) and (2. 33)). In the case of classically forbidden transition, the reduced scattering matrix element S_{ij}^{R} should be used (see Eqs.(2. 34) and (2. 45)). Once the total wave function $\psi(t)$ is known, the transition amplitude for any transition can be simply calculated by taking the projection of the above total wave function $\psi(\mathbf{r},t)$ onto the final state $\psi_f(\mathbf{r})$. It should be noted that if a classical trajectory goes around a conical intersection, the geometrical phase, or Berry phase[49] should be added.

In the case of photo-absorption the total absorption cross section is given by

$$\sigma(\omega) = \frac{2\pi\alpha a_0^2\omega}{\hbar}\int_{-\infty}^{\infty}dt\exp[iEt/\hbar] < \psi(0)|\psi(t) >, \qquad (3.\ 9)$$

where α, a_0 and ω are fine structure constant, Bohr radius, and light frequency, respectively. The wave function $\psi(0)$ represents the initial state on the excited potential energy surface and is given by

$$|\psi(0) >= \mu|\phi_i >, \qquad (3.\ 10)$$

where ϕ_i and μ represent the initial state on the ground potential energy surface and the transition dipole moment. The total wave function $\psi(t)$ is calculated by the above mentioned Herman-Kluk type IVR method. When the photo-excited state is nonadiabatically coupled with some other excited states through conical intersections, this $\psi(t)$ can be calculated by the ZN-HKSCIVR method. Photo-absorption of NH_3 described in the next Section 4.2 corresponds to this case. Eq.(3. 9) indicates that the total absorption cross section is given by the Fourier transform of the auto-correlation function $< \psi(0)|\psi(t) >$[50].

In the above treatment of nonadiabatic transition, it is assumed that the energy at the transition point is given by that of classical trajectory of the center of each frozen Gaussian wave packet. More accurate treatment to take into account the fact that each frozen Gaussian has energy distribution is to use the energy normalized

17

eigenfunction expansion method[51]. The frozen Gaussian wave packet just before the transition is expanded in terms of the energy normalized eigenfunction on the corresponding potential energy surface. The expansion coefficient is transformed into the new one by multiplying the Zhu-Nakamura transition amplitude. The wave function right after the transition is obtained from the new coefficients and the energy normalized eigenfunctions on the new potential energy surface. In actual applications the simplified version with use of the energy of the center of each frozen Gaussian wave packet would be good enough.

3.3. Reaction rate constant of nonadiabatic dynamics

The nonadiabatic transition state theory (NA-TST) has been developed by many authors by using the perturbative treatment of diabatic coupling or the Landau-Zener formula (for instance, [52, 53, 54, 55, 56]). Since electron transfer process is one of the most typical nonadiabatic dynamics, the theory has also been developed for the process[57, 58, 59] basically by using the perturbation theory. The Zhu-Nakamura theory can improve the situation by covering the whole range of coupling strength from diabatic to adiabatic regime[60]. The semiclassical instanton theory has also been extended to nonadiabatic dynamics[61].

Here, we employ the ordinary formulation of thermal rate constant, which is given by

$$k(T) = \frac{1}{Z_r} \frac{1}{2\pi\hbar} \int_0^\infty dE \exp[-\beta E] N(E), \qquad (3.\ 11)$$

where T is the temperature with $\beta = 1/\kappa T$, Z_r is the partition function of reactants and $N(E)$ is the cumulative reaction probability. In the case of nonadiabatic dynamics, the latter is defined by

$$N(E) = \frac{1}{(2\pi\hbar)^{F-1}} \int d\vec{p}\,d\vec{q}\,\delta[E - H(\vec{p}, \vec{q})]\delta[f(\vec{q})](\vec{\nabla} f \cdot \vec{p}) P_{ZN}(E_\perp(\vec{q})), \qquad (3.\ 12)$$

where F is the number of dimension, $f(\vec{q}) = 0$ defines the dividing surface, which is actually taken to be the crossing seam surface, and $E_\perp(\vec{q})$ represents the kinetic energy in the direction perpendicular to the crossing seam surface. The momentum vector is now expressed as $\vec{p} = (p_{\parallel(1)}, , , , p_{\parallel(F-1)}, p_\perp)$, where $\vec{p}_\parallel$ and $p_\perp$ are the momenta parallel and perpendicular to the crossing seam surface, respectively. By introducing the energies $E_{\parallel(j)} = p_{\parallel(j)}^2/2$ and $E_\perp = p_\perp^2/2$, where the mass is assumed to be unity or the momenta are mass scaled, and using $\vec{\nabla} f \cdot \vec{p} = p_\perp$ and the energy conservation,

$$E = H = E_\perp + E_\parallel^{[F-2]} + E_{\parallel(F-1)} + V(\vec{q}_\dagger) \qquad (3.\ 13)$$

with

$$E_\parallel^{[K]} \equiv \sum_{j=K+1}^{F-1} E_{\parallel(j)}, \qquad (3.\ 14)$$

18

the integrals over momenta can be rewritten as

$$\text{Int}(E) \equiv \int dp_\perp p_\perp \prod_{j=1}^{F-1} \int dp_{\parallel(j)} \delta(E - H)$$

$$= (\frac{1}{\sqrt{2}})^{F-1} \int_{-V}^{E-V} dE_\perp \prod_{j=1}^{F-2} \int_0^{E_\parallel^{[j-1]}} dE_{\parallel(j)} \frac{1}{\sqrt{E_{\parallel(j)}}} \frac{1}{\sqrt{E_{\parallel(F-1)}}} \qquad (3.\ 15)$$

with $E_{\parallel(F-1)} = E_\parallel^{[F-3]} - E_{\parallel(F-2)}$. Using the beta function,

$$B(p, q) = \int_0^1 dt t^{p-1} (1 - t)^{q-1}, \qquad (3.\ 16)$$

we obtain

$$\text{Int}(E) = \int_{-V}^{E-V} dE_\perp (E - E_\perp - V)^{(F-3)/2} \prod_{m=1}^{F-2} B(\frac{1}{2}, \frac{m}{2}), \qquad (3.\ 17)$$

where

$$\prod_{m=1}^{F-2} B(\frac{1}{2}, \frac{m}{2}) = \frac{[\Gamma(1/2)]^{F-1}}{\Gamma[(F-1)/2]}. \qquad (3.\ 18)$$

Then the cumulative reaction probability, i.e., the micro-canonical rate constant, is finally given by

$$N(E) = (2\pi\hbar)^{-F+1} \frac{\pi^{(F-1)/2}}{2^{(F-1)/2} \Gamma[(F-1)/2]} \int d\vec{q} \delta[f(\vec{q})]$$

$$\times \int_{-V}^{E-V} dE_\perp (E - E_\perp - V)^{(F-3)/2} P_{ZN}(E_\perp). \qquad (3.\ 19)$$

Since the order of integration over E and $E_\perp$ can be changed as,

$$\int_0^\infty dE \int_{-V}^{E-V} dE_\perp = \int_{-V}^\infty dE_\perp \int_{E_\perp+V}^\infty dE, \qquad (3.\ 20)$$

the thermal rate constant is finally obtained as

$$k(T) = \frac{1}{Z_r} \frac{1}{2\pi\hbar} \frac{1}{(8\pi\beta\hbar^2)^{(F-1)/2}} \int d\vec{q}_\dagger \int_0^\infty dE_s \exp[-\beta E] P_{ZN}(E_s), \qquad (3.\ 21)$$

where $E_s = E_\perp + V_\dagger$, $\vec{q}_\dagger$ represents the $(F-1)-$dimensional coordinate space and $V_\dagger$ is the potential along the crossing seam. The rate constant can be simply rewritten as

$$k(T) = \frac{1}{Z_r} \frac{1}{2\pi\beta\hbar} \frac{1}{(8\pi\beta\hbar^2)^{(F-1)/2}} \int d\vec{q}_\dagger P_{ZN}(\beta; \vec{q}_\dagger), \qquad (3.\ 22)$$

where

$$P_{ZN}(\beta; \vec{q}_\dagger) = \beta \int dE_s \exp[-\beta(E_s - V_\dagger)] P_{ZN}(E_s; \vec{q}_\dagger). \qquad (3.\ 23)$$

The minimum energy crossing point $(\vec{q}_\dagger^{(0)})$ (MECP) approximation is often employed, in which the transition is assumed to occur only at $(\vec{q}_\dagger^{(0)})$[53, 60, 55, 56]. In this case the rate constant is approximated by

$$k(T) = \frac{1}{Z_r}\frac{1}{2\pi\beta\hbar}\frac{1}{(8\pi\beta\hbar^2)^{(F-1)/2}}P_{ZN}(\beta; \vec{q}_\dagger = \vec{q}_\dagger^{(0)})\int d\vec{q}_\dagger \exp[-\beta(V_\dagger)], \qquad (3.\ 24)$$

As is well known, electron transfer is one of the most famous nonadiabatic chemical processes and the Marcus theory is most celebrated[57, 58]. The Marcus theory is based on the first order perturbation of electronic coupling. By using the ZN theory, we can improve this theory (see (b) and (e) of [60]). Since the electron transfer is formulated in the free energy space, we introduce the free energy profile by (see Eq.(3. 12))

$$\exp[-\beta F_r(\xi)] = \int d\vec{q}\exp[-\beta V_r(\vec{q})]\delta[\xi - f(\vec{q})]|\vec{\nabla}f(\vec{q})|, \qquad (3.\ 25)$$

where the index r represents "reactant", ξ is the free energy and $\xi = \xi_0 = f(\vec{q})$ defines the crossing seam surface. As in the case of Marcus theory, we assume the parabolic approximation,

$$F_r(\xi) = \frac{1}{2}\omega^2(\xi - \xi_{01})^2, \quad F_p(\xi) = \frac{1}{2}(\xi - \xi_{02})^2 + \Delta G, \qquad (3.\ 26)$$

where F_p is the product potential, ξ_{01} (ξ_{02}) is the position of the donor (acceptor) free energy minimum, and ΔG represents the exothermicity. The crossing point ξ_0 is given by

$$\xi_0 = \frac{1}{2}(\xi_{01} + \xi_{02}) + \frac{\Delta G}{\omega^2\delta\xi_0} \qquad (3.\ 27)$$

with $\delta\xi_0 = \xi_{01} - \xi_{02}$. The Marcus formula is given by

$$k_{Marcus}(T) = \frac{H_{DA}^2}{\hbar}\sqrt{\frac{\pi\beta}{\lambda}}\exp[-\beta\frac{(\lambda + \Delta G)^2}{4\lambda}], \qquad (3.\ 28)$$

where

$$\lambda = \frac{1}{2}\omega^2(\delta\xi_0)^2. \qquad (3.\ 29)$$

Then the improved formula is given by

$$k(T) = \kappa k_{Marcus}(T), \qquad (3.\ 30)$$

where

$$\kappa = \frac{\hbar}{2\pi H_{DA}^2}\sqrt{\frac{\lambda}{\pi\beta}}\bar{P}(\beta; \xi_0). \qquad (3.\ 31)$$

The energy averaged transition probability $\bar{P}(\beta; \xi_0)$ is given by

$$\bar{P}(\beta; \xi_0) = \beta\int_0^\infty dE \exp[-\beta E]P_{ZN}(E; \xi_0). \qquad (3.\ 32)$$

Both of Marcus's normal (NT type) and inverted (LZ type) cases can be treated with use of the corresponding ZN probability formulas.

3.4. How to treat the effects of environment

The environmental effects are quite crucial to comprehend chemical dynamics in wet chemistry. The so called dielectric medium model or the polarized continuum model (PCM)[62, 63, 64] has been widely employed to take into account the solvation effects. The solvent in this model is treated as a continuum medium with a constant permittivity and the solute molecule is put in a certain empirical cavity. The dynamical solvation effect cannot be treated by the PCM model, unfortunately. In this model, the liquid structure is discussed in terms of the radial distribution function (RDF). Chandler and coworkers have developed the reference interaction site model (RISM) theory[65, 66] based on the Ornstein-Zernike equation. Hirata and coworkers combined this RISM theory with quantum chemistry. This is called RISM-self consistent field (RISM-SCF) approach[67, 68, 69]. Since the solution structure and electronic states are iteratively optimized in RISM-SCF, the solvation effects are reasonablly well taken into account by using the quantum chemical calculations. The RDF obtained from the RISM-SCF method is, however, one-dimensional averaged distribution in spite of the fact that the dynamical solvation effect occurs in three-dimensional space. One can employ the three-dimensional RISM-SCF method, which has been extended to the simulation of dynamics[70]. But this is very much time-consuming, unfortunately.

On the other hand, the molecular mechanical (MM) simulation is quite popular in molecular dynamics of condensed matter. Analytical potential functions with empirical parameters are used in the MM method. One of the most famous force fields is AMBER[71, 72, 73]. The computational cost of the MM method is proportional to the square of number of atoms, and it could be reduced by the neighbor-list method[74]. This is quite a reasonable approach for obtaining the statistical information. The target of the conventional MM approach is therefore focused on the electronic ground state of the system. The conventional formulas and parameters in this MM approach are designed to reproduce equilibrium molecular conformation in the electronic ground state. Furthermore, the periodic boundary condition (PBC) is used to take into account the solution or crystal environment, and the solvent is represented as a finite system surrounded by its replicas. The minimum-image (MI) convention and the cutoff-radius are also introduced to calculate the total energy and force in spite of the fact that the Coulombic interaction goes to zero very slowly. In order to treat the long-range electrostatic interaction, the Ewald summation method has been implemented. The MD simulation together with the Ewald summation method can achieve explicit treatment of the long range Coulombic interaction compared to the implicit way of treatment by the RISM theory (see Fig.5)[75, 76, 77].

3.4.1. QM/MM method

Morokuma *et al.* have proposed a sophisticated approach for treating large chemical systems by using quantum chemical and molecular mechanical (QM/MM) hybrid-
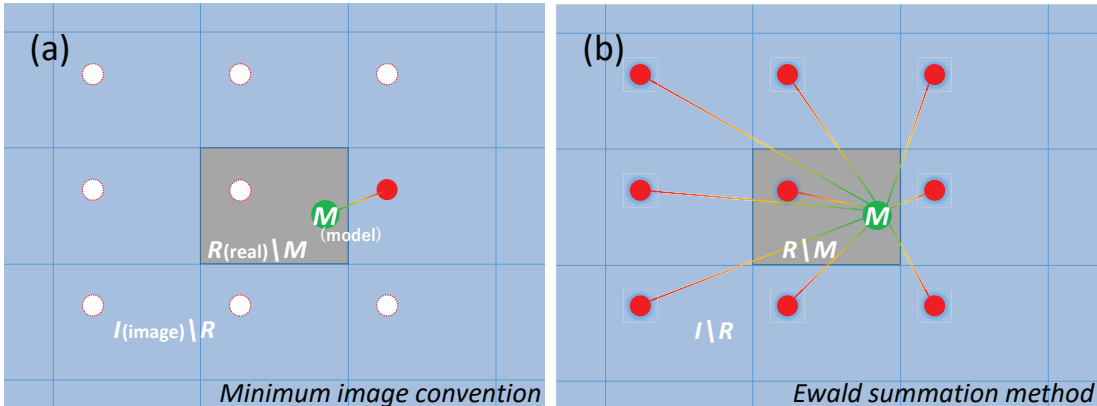
Figure 5: The difference between (a) MI convention and (b) Ewald summation method. The green and red circles represent particles in the region M and in its outside, respectively. The lines connecting circles indicate interactions taken into account.

model known as ONIOM (our Own N-layer Integrated molecular Orbitals and molecular Mechanics) theory[78, 79]. The potential energy of the chemical reaction part (QM layer) is computed by *ab initio* quantum chemical calculation, and the remaining nonreactive surrounding part (MM layer) is given by an empirical molecular mechanics (MM) potential. The ONIOM potential energy is defined by the extrapolation form,

$$E_{\text{ONIOM}} = E_{\text{real}}^{\text{MM}} + E_{\text{model}}^{\text{QM}} - E_{\text{model}}^{\text{MM}}, \tag{3. 33}$$

where "real" and "model", respectively, refer to the full system and the QM layer. $E_{\text{real}}^{\text{MM}}$ is the MM potential energy of the full system, $E_{\text{model}}^{\text{QM}}$ is the QM energy of the model layer, and $E_{\text{model}}^{\text{MM}}$ is the MM energy of the same model layer. In this approach there are two methods to compute $E_{\text{model}}^{\text{MM}}$ and $E_{\text{model}}^{\text{QM}}$; one is based on the mechanical embedding (ME) method, while the other is based on the electrostatic embedding (EE) method[79].

The use of molecular dynamics (MD) simulation to comprehend chemical dynamics is quite popular nowadays. In the on-the-fly MD (direct dynamics) simulation, the potential energy and its force are provided by *ab initio* quantum chemical calculations at each time-step. The ONIOM-MD simulation can be performed in the similar way[80, 81]. If the boundary between reaction center and its surrounding environment is clearly known a priori, the ONIOM-MD simulation method can be applied in a straightforward way. If this is not the case and the boundary is not pre-

dictable, the exchange-algorithm of solvent molecules (ONIOM-XS) and the adaptive multiscale QM/MM-MD method can be used[82, 83, 84]. Namely, the ONIOM method enables us to deal with large complex chemical and biological systems.

It is known now that various quantum mechanical effects play key roles even in complex systems [85]-[94] and that the polarized continuum model (PCM) cannot necessarily reproduce the effects. York and coworkers have extended the particle-mesh Ewald summation method (PME) so as to be combined with QM/MM[95]. The ONIOM scheme[78, 79] is superior to the simple QM/MM scheme with respect to the calculation of the interaction between QM and MM layers; thus the PME method should be incorporated into the ONIOM scheme[96, 97].

3.4.2. Particle-mesh Ewald summation method

A.**Formulas of force field**
The AMBER force field is composed of five terms, which are energies of (i) bond, (ii) angle, (iii) dihedral angle, (iv) van der Waals interaction, and (v) Coulombic interaction:

$$V = \sum_{\text{bonds}} k_r(r - r_{eq})^2 + \sum_{\text{angles}} k_\theta(\theta - \theta_{eq})^2 + \sum_{\text{dihedrals}} \frac{V_n}{2}\left[1 + \cos(n\varphi - \gamma)\right]$$
$$+ \sum_{i<j}\left[\frac{A_{ij}}{R_{ij}^{12}} - \frac{B_{ij}}{R_{ij}^6}\right] + \sum_{i<j}\left[\frac{q_i q_j}{\varepsilon R_{ij}}\right], \quad (3.\ 34)$$

where r, θ, ϕ and R_{ij} are the bond length, bond angle, dihedral angle and the distance between atom i and j, respectively. The parameters r_{eq} and θ_{eq} refer to bond distance and bond angle at equilibrium molecular geometry, k_r and k_θ are the respective force constants. The angle γ is the offset of rotation, q_i and q_j are atomic charges of atoms i and j, and ϵ is 4π times of permittivity of vacuum.

If we use the periodic boundary condition, the Coulombic interaction is rewritten as
$$U = \frac{1}{2}\sum_i \sum_{j\neq i} \frac{q_i q_j}{|\mathbf{R}_i - \mathbf{R}_j|} + \frac{1}{2}\sum_{\mathbf{N}\neq 0}\sum_i \sum_{j\neq i} \frac{q_i q_j}{|\mathbf{R}_i - \mathbf{R}_j - \mathbf{N}|}, \qquad (3.\ 35)$$

where $\mathbf{R_i}$ and $\mathbf{R_j}$ are the coordinates of atoms i and j, respectively, and $\mathbf{N}$ is the origin of replica, namely, $\mathbf{N} = \xi\mathbf{a} + \eta\mathbf{b} + \zeta\mathbf{c}$, where ξ, η, ζ are integers and $\mathbf{a}$, $\mathbf{b}$, $\mathbf{c}$ are the lattice vectors.

B.**Definition of model**, **real and image layers**
The three-layer model is defined in the ONIOM approach as shown in Fig.6. The layers M (model) and R (real) represent the reaction center and the environment, respectively. The unit cell in the present treatment is R. The surrounding image layer denoted by I is provided by the periodic replicas of the real layer (R). We have therefore the relationship $M \subset R \subset I$. The subspace $R\backslash M(= R - M)$ represents the outer space of M within R and is the region where the electrostatic embedding
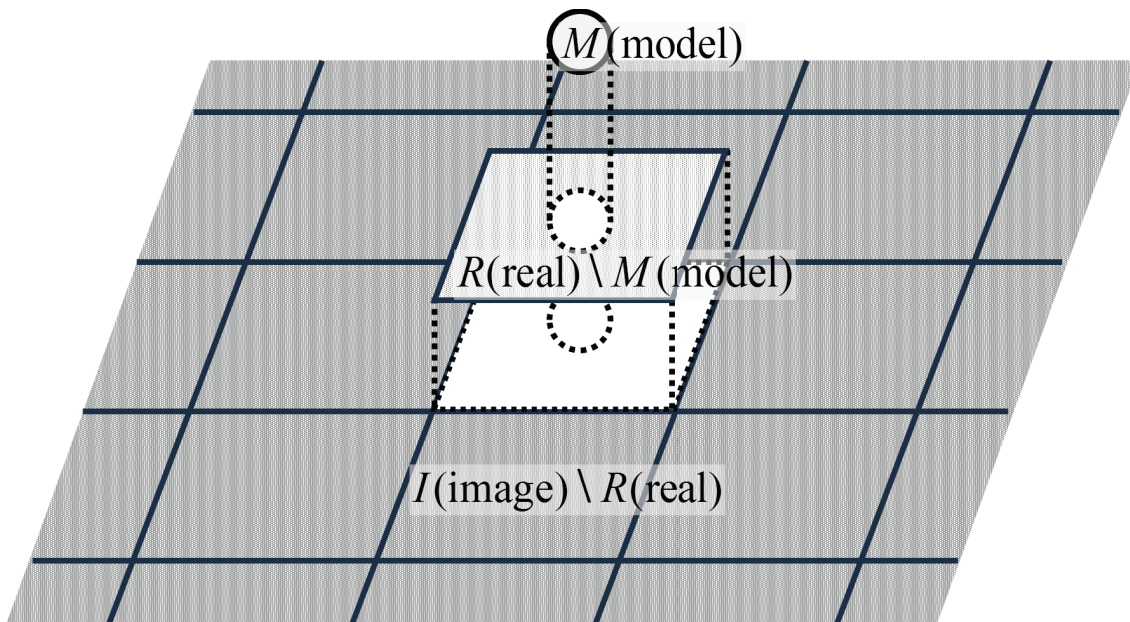
scheme is employed.

Figure 6: Three-layer model based on the ONIOM scheme. The unit cell is composed of M (model) and R (real), and the image layer I is composed of the periodic replicas of R.

C. The original ONIOM scheme
(i) Coulombic interaction

In the original ONIOM scheme, the PBC is not employed and the total Coulombic energy is given by a finite sum

$$U = \frac{1}{2} \sum_A q_A \sum_{B(A \neq B)} \frac{q_B}{r_{AB}}, \qquad (3.\ 36)$$

where q_A and q_B are effective charges of particles A and B ($\in R$), and $r_{AB} = |\mathbf{r}_B - \mathbf{r}_A|$. If both A and B belong to M, the interaction is taken into account by quantum chemical calculations (QM). In the case that $A \in M$ and $B \in R \backslash M$, on the other hand, the pairwise interaction is directly estimated as given above, which is called the mechanical embedding (ME) method. In the more sophisticated procedure called electrostatic embedding (EE) method, the following modified one-electron operator for the i-th electron is used in the electronic Hamiltonian of the subspace M:

$$h_i^{\text{QM}} - \sum_{B \in R \backslash M} \frac{q_B}{r_{iB}}, \qquad (3.\ 37)$$

where h_i^{QM} is the original one-electron operator. This EE method is employed in the following sections unless otherwise noted.

24

(ii) van der Waals (vdW) interaction
The vdW interaction is expressed as

$$U_{VDW} = \sum_A \sum_{B(A \neq B)} \left[\left(\frac{A_{AB}}{r_{AB}} \right)^{12} - \left(\frac{B_{AB}}{r_{AB}} \right)^6 \right]. \tag{3.38}$$

As mentioned above, the cut off procedure is employed and the summation in Eq.(3. 38) is finite in the ONIOM scheme. The parameters A_{AB} and B_{AB} are given by AMBER force field[71].

The ONIOM energy is finally given by Eq.(3. 33) which is pictorially shown in Fig.7(a). The ONIOM energy gradient that is needed for classical trajectory calculation is straightforwardly obtained from Eq.(3. 33) by term-wise differentiation as

$$\frac{\partial E_{\text{ONIOM}}}{\partial \mathbf{R}} = \frac{\partial E_{\text{real}}^{\text{MM}}}{\partial \mathbf{R}} + \frac{\partial E_{\text{model}}^{\text{QM}}}{\partial \mathbf{R}} - \frac{\partial E_{\text{model}}^{\text{MM}}}{\partial \mathbf{R}}. \tag{3.39}$$

D. Particle-mesh Ewald summation approach with use of the ONIOM scheme

(i) Coulombic interaction
The Coulombic interaction defined in the scheme of periodic boundary condition (PBC) given by Eq.(3. 35) is rewritten as

$$U_{Ewald} = \frac{1}{2} \sum_{\mathbf{N}} \sum_A q_A \sum_{B(\neq A)} \frac{q_B}{r_{AB\mathbf{N}}}, \tag{3.40}$$

where the lattice vector of the cell is $\mathbf{N}$, and $r_{AB\mathbf{N}} = |\mathbf{r}_B - \mathbf{r}_A - \mathbf{N}|$ is the distance between particle $A \in R$ and the particle $B \in I \backslash R$. This can be divided into the following two terms according to the particle-mesh Ewald summation (PME) approach[76, 77],

$$U_{Ewald} = U_{int} + U_{ext}. \tag{3.41}$$

The first term U_{int} represents the interactions in the unit cell,

$$U_{int} = \frac{1}{2} \sum_A q_A \sum_{B(\neq A)} \frac{q_B}{r_{AB}}, \tag{3.42}$$

where A and $B \in R$. This term is the same as the corresponding energy in the ONIOM approach and is estimated by the quantum chemical calculation within the EE scheme.

On the other hand, U_{ext} represents the interaction between the unit cell (R) and the replicas($I \backslash R$),

$$U_{ext} = \frac{1}{2} \sum_{\mathbf{N}(\neq \mathbf{0})} \sum_A q_A \sum_B \frac{q_B}{r_{AB\mathbf{N}}}, \tag{3.43}$$

where $A \in R$ and $B \in I\backslash R$.

When $A \in R$ and $B \in R$, the computational procedure of Coulombic interaction is same as that in the ONIOM scheme. The Coulombic potential energies for $B \in I\backslash R$ can only be taken into account in the PME-ONIOM scheme. In the case of $A \in R\backslash M$, the Coulombic potential energies are calculated by PME wherever the particle B is located. The Coulombic potential energy for $A \in I\backslash R$ is not calculated wherever B is located.

(ii) vdW interaction
The vdW interaction energy in PBC is given by

$$U_{VDW} = \sum_{\mathbf{N}} \sum_{A} \sum_{B(\neq A)} \left[(\frac{A_{AB}}{r_{AB\mathbf{N}}})^{12} - (\frac{B_{AB}}{r_{AB\mathbf{N}}})^{6} \right]. \qquad (3.\ 44)$$

Since U_{VDW} decays rapidly with the distance, the summation over $\mathbf{N}$ is taken only over the nearest neighbor replicas, namely $|\mathbf{N}| = \pm 1$. This is the so called minimum image (MI) convention. The parameters A_{AB} and B_{AB} are obtained also from the general AMBER force field[71, 72, 73]. When $A \in R$ and $B \in R$, the computational method is same as that in the original ONIOM scheme. The vdW potential energy for $B \in I\backslash R$ is calculated by the MM method. But this interaction could usually be cut off, since the subspace $I\backslash R$ is quite far from M.

In the case of $A \in R\backslash M$ and $B \in R$, the interaction is calculated by the MM method. The interaction for $B \in I\backslash R$ is also calculated by MM, but the summation is taken over the minimum image (MI) ($|\mathbf{N}| = \pm 1$).

The PME-ONIOM procedure is summarized as follows[96]:

- E $_{\text{real}}^{\text{MM}}$ by the PME approach.

- E $_{\text{model}}^{\text{MM}}$ by the direct summation of the interaction energy.

- E $_{\text{model}}^{\text{QM}}$ by the quantum chemical calculation with use of the electrostatic embedding scheme.

Since the periodic boundary condition (PBC) provides the additional interaction energy ΔE between the model (M) and its outside, the PME-ONIOM energy is finally given by

$$E_{\text{PME-ONIOM}} = E_{\text{real}}^{\text{MM}} + E_{\text{model}}^{\text{QM}} - E_{\text{model}}^{\text{MM}} + \Delta E \qquad (3.\ 45)$$

which is pictorially shown in Fig.7. The orange-colored part circumscribing the green QM part is of electrostatic embedding (EE) scheme given by Eq.(3. 37); the quantum chemical calculation is performed by directly taking into account the Coulombic interaction between the electron in the subspace M and the charge q_B in $R\backslash M$ and $I\backslash R$, where the polar solvent molecules are described by charge distribution. On
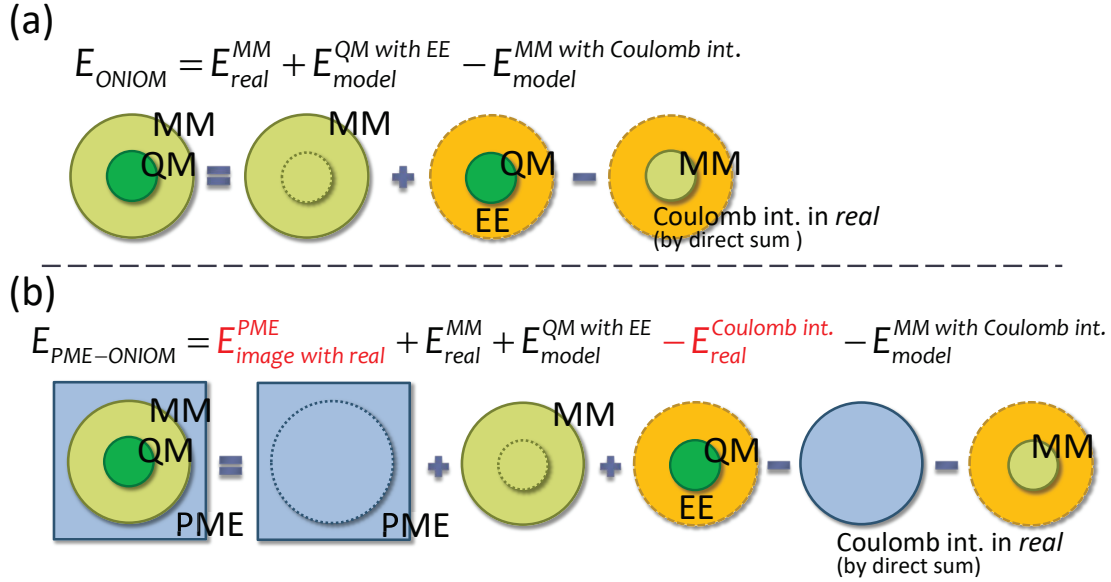
(a)

$$E_{ONIOM} = E_{real}^{MM} + E_{model}^{QM\ with\ EE} - E_{model}^{MM\ with\ Coulomb\ int.}$$

MM
QM
MM
MM
QM
EE
MM
Coulomb int. in *real*
(by direct sum)

(b)

$$E_{PME-ONIOM} = E_{image\ with\ real}^{PME} + E_{real}^{MM} + E_{model}^{QM\ with\ EE} - E_{real}^{Coulomb\ int.} - E_{model}^{MM\ with\ Coulomb\ int.}$$

MM
QM
PME
PME
MM
QM
EE
MM
Coulomb int. in *real*
(by direct sum)

Figure 7: The pictorial scheme of (a) original ONIOM scheme with electrostatic embedding (EE) and (b) PME-ONIOM approach with EE. These figures are based on the practical scheme rather than the above mentioned theoretical concept.

the other hand, the QM calculation without the EE scheme is carried out by the mechanical embedding (ME) scheme. Thus, the PME method makes it possible for the Coulombic interaction to directly affect the QM part.

The difference between the original ONIOM scheme and the PME-ONIOM scheme is the existence of the term of ΔE. The polarity of solution can be properly taken into account by the present EE scheme. In the present PME-ONIOM scheme, the subspace $I\backslash R$ may be divided into two layers: one is described by the electrostatic embedding method ($R\backslash M$) and the other is described by the mechanical embedding method ($I\backslash R$). In this sense the present PME-ONIOM scheme can be combined with the three-layered ONIOM. In the same way as in Section 3.4.2 **C**, the energy gradient is straightforwardly calculated from

$$\frac{\partial E_{\text{PME-ONIOM}}}{\partial \mathbf{R}} = \frac{\partial E_{\text{real}}^{\text{MM}}}{\partial \mathbf{R}} + \frac{\partial E_{\text{model}}^{\text{QM}}}{\partial \mathbf{R}} - \frac{\partial E_{\text{model}}^{\text{MM}}}{\partial \mathbf{R}} + \frac{\partial \Delta E}{\partial \mathbf{R}}. \qquad (3.\ 46)$$

4. Clarification of dynamics

4.1. Reactions in tri-atomic systems

Applications of the ZN-TSH method to the reactions in tri-atomic systems are reported here by taking DH_2^+ and CH_2 systems as examples. The DH_2^+ is the well known most basic system that has a conical intersection at infinity with the crossing seam almost parallel to the reaction coordinate. In this kind of simple systems we can use analytical expressions of potential energy surfaces. The potential energy surfaces used for DH_2^+ are the diabatic representation developed by Ushakov *et al.*[98]. In the actual TSH calculations the adiabatic potentials are used by diagonalizing the diabatic ones and the crossing seam surface is expressed by analytical functions. Fig.8 shows numerical results of the cumulative reaction probability for the specified initial rovibrational state for $H_2(v = 1, j = 2) + D^+ \rightarrow HD^+ + H$[99]. QM is the result of quantum mechanical numerical solutions of coupled Schrödinger equations. The new (old) TSH means the TSH calculations with use of the ZN (LZ) formulas. Since resonances are not the target of interest here, we can say that the ZN-TSH works well to reproduce the overall reaction probability. It should be noted that the nonadiabatic transitions are classically forbidden when the vibrational quantum number v is less than or equal to 3. This means that the ZN-TSH works well even for classically forbidden transitions. It should also be noted that the LZ-TSH does not work even at high energies. This is because the transitions may become classically forbidden due to energy transfer in the multi-dimensional space. The cross section calculations for $H^+ + D_2$ and $D^+ + H_2$ are carried out with use of the Zhu-Nakamura theory by Li and Han[100].

The second example is the reaction $C + H_2(v = 1, j = 0) \rightarrow CH + H$. This has a conical intersection in the reaction zone and both LZ and NT types of transitions occur. The model potential energy surfaces are constructed by using the DIM (diatomics in molecule) method[48]. Here the generalized TSH method explained in Section 3.1 is employed without using analytical expression of crossing seam surface. The approximate way of estimating nonadiabatic coupling vector with use of Hessian is demonstrated to work well. One of the numerical results is shown in Fig.9. This shows the cumulative reaction probability for the above mentioned process. There are many resonances because of the deep potential well in the ground state potential energy surface. Again resonances are not the target of interest. The ZN-TSH method works acceptably well. The open symbol represents the result with use of the approximate nonadiabatic coupling vector.

4.2. Absorption spectrum of NH_3

The photoabsorption dynamics of ammonia (NH_3) is investigated by the ZN-HKSCIVR approach with the full dimensional degrees of freedom taken into account[101]. It is well-known that the progressions in the umbrella mode (ν_2) in the $S_1 \leftarrow S_0$ absorp-
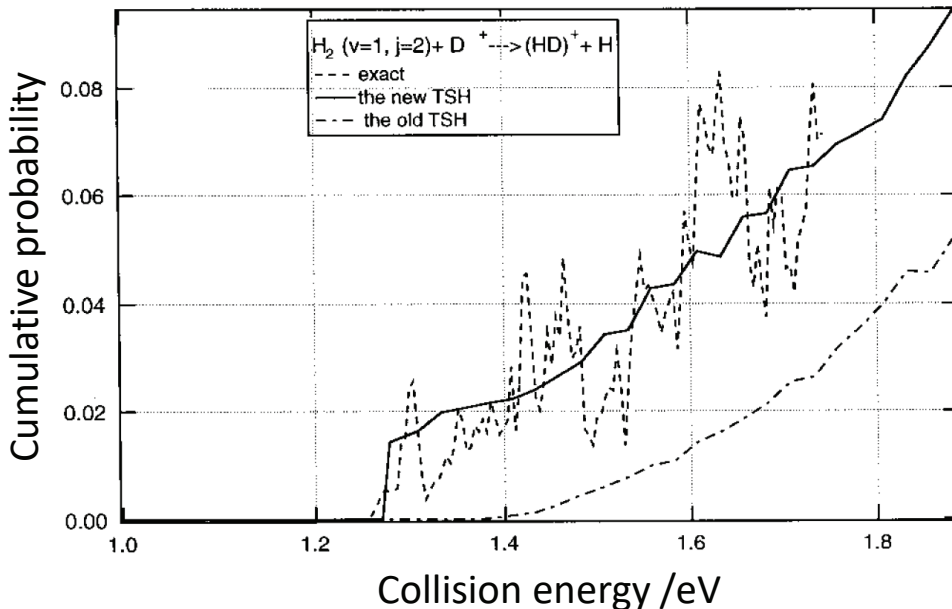
Figure 8: Cumulative reaction probability for the specified initial rovibrational state ($v = 1, j = 2$). The new (old) TSH means the present results with use of the Zhu-Nakamura (Landau-Zener) formulas. Reproduced from Ref.[99] by permission of American Institue of Physics (AIP).

tion band are observed in the Franck-Condon region [102, 103, 104]. The scenario of photodissociation of ammonia molecule is as follows:

(1) The excited molecule is trapped by the shallow well just after excitation to S_1.

(2) The ν_2-progression features the broad peaks partly due to tunneling effect by the predissociation in the shallow well.

(3) The excited molecule passes through the conical intersection between S_1 and S_0 along the dissociation pathway to NH_2 + H.

Since this is a problem of spectrum, ZN-HKSCIVR is a suitable approach. The

Table 1: The vertical excitation energy for $S_1 - S_0$ of NH_3 with use of two different methods

Thoery	Vertical excitation energy
MRCI/aug-cc-pVDZ	6.66
SA-CASSCF/aug-cc-pVDZ	5.93

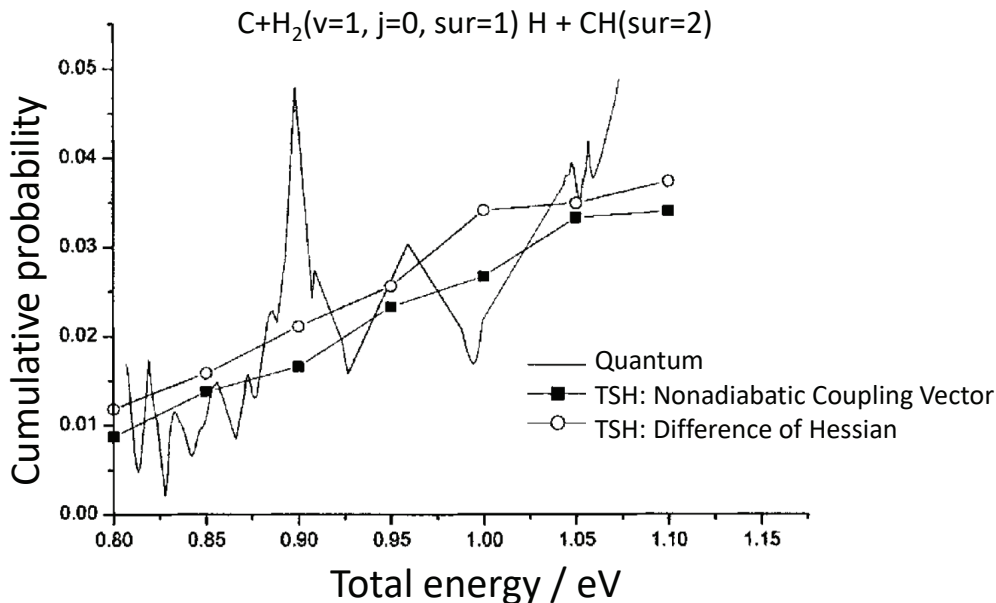state-averaged 8-electron and 7-orbital complete active space self-consistent field

Figure 9: Cumulative reaction probability for the specified initial rovibrational state $(v = 1, j = 0)$. The solid (open) square is the result with use of the proper nonadiabatic coupling vector (approximate vector obtained from Hessian. Reproduced from Ref.[48] by permission of AIP.

(CAS(8e,7o)-SCF) scheme was used in the *ab initio* part of the on-the-fly dynamics. The Hessian matrices are required to propagate the frozen Gaussian wavepackets, as explained in Section 3.2. To estimate the error due to SA-CASSCF in the S_1-S_0 excitation energy, the MRCI calculation was performed at the same level of basis set. The result is listed in Table 1. Since the estimated error is 0.73 eV, the result for ν_2-progression is shifted by this amount.

Figure 10 shows the full-dimensional spectrum comprised by forty trajectories. It should be noted that the nonadiabatic transition along the dissociation path provides the background broad peak that is missing in the one-surface treatment done by Guo *et al.* [104]. Table 2 shows the peak energies of the ZN-HKSCIVR and experimental spectra. The experimental measurement was performed at 16 K [102]. The peak energies of the present theoretical results reasonably well agree with the experimental data. The intervals of the peaks of ND_3 are clearly smaller than those of NH_3. This indicates that the quantization of vibrational motions are well represented by the semiclassical method. The energy difference between the theory and experiment is approximately 300cm^{-1}. Another significant isotope effect is the narrowing of peak widths observed experimentally[102, 103]. In this sense it would be interesting to improve the present treatment by taking into account the quantum mechanical tunneling effect. This can be done by applying the newly developed method[45].
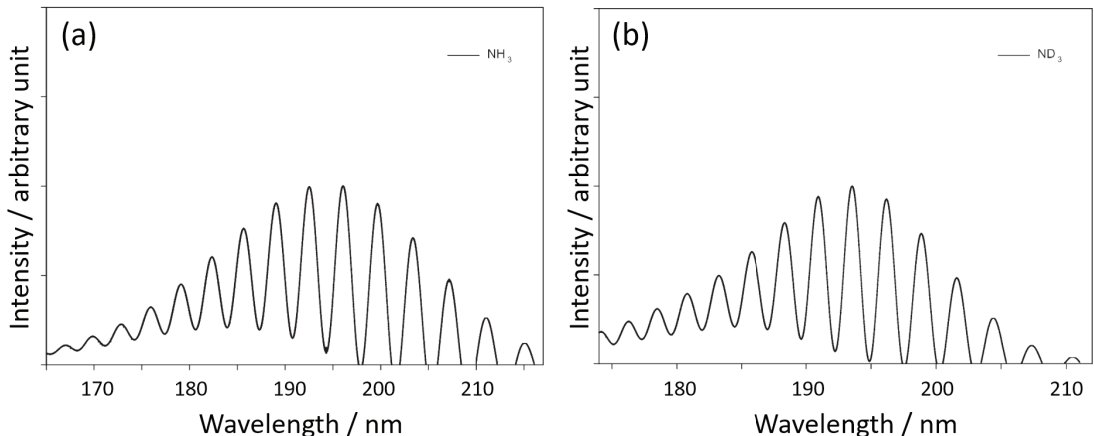
Figure 10: Photoabsorption spectra of (a) NH_3 and (b) ND_3

4.3. Reaction rate of electron transfer

The nonadiabatic transition state theory (NA-TST) explained in Section 3.3 has been applied to electron transfer processes. The first example is to demonstrate that the NA-TST based on the Zhu-Nakamura theory works well over the whole range of electronic coupling strength (see (c) of [60]). Fig.11 displays the calculated results of five different approaches as a function of electronic coupling (H_{AB}) in the unit of ω at low temperature $T = 0.3\omega$, where $\omega = 500$ cm^{-1} is the frequency of harmonic oscillators. The potential system used is a simple one-dimensional model of two shifted harmonic oscillators, the parameters of which are taken from Ref.[105]. The potential energy at crossing V_0, the effective mass m, and the exothermicity ΔG are $V_0 =$1500 cm^{-1}, m = 1836 m$_e$. and $\Delta G = 0$, respectively. It should be noted that the simplicity of the model does not destroy the generality. As is seen, the present NA-TST theory based on the ZN theory (solid line) agrees very well with the exact quantum mechanical results (dots) in the whole range of the coupling strength. The Bixon-Jortner theory[58] (dot line) works well in the weak coupling regime ($H_{AB} < 0.2\omega$), but fails at larger couplings. The worse results by the Marcus theory (dash line) and by the Marcus formula with use of the LZ (dash-dot line) probability indicate the importance of nonadiabatic tunneling. Namely, not only the nuclear tunneling but also the coupling between electronic and nuclear motions play crucial roles.

The second example is the reproduction of the experiment done by Nelsen *et. al*[106]. They measured the electron transfer rate of 2,7-dinitronaphthalene in three

Table 2: The peak positions (ν_2-progression) of theoretical and experimental data for NH_3 and ND_3.

	NH_3			ND_3	
Band	Exp./cm^{-1}	Theo.*/cm^{-1}	Band	Exp./cm^{-1}	Theo.*/cm^{-1}
0^0	46222	46495	0^0	46701	46823
2^1	47057	47374	2^1	47369	47538
2^2	47964	48273	2^2	48052	48233
2^3	48869	49172	2^3	48697	48928
2^4	49783	50112	2^4	49357	49602
2^5	50730	51012	2^5	50062	50277
2^6	51656	51952	2^6	50748	50971
2^7	52543	52892	2^7	51451	51666
2^8	53469	53872	2^8	52168	52381
2^9	54454	54853	2^9	52874	53097
2^{10}	55380	55834	2^{10}	53582	53832
2^{11}	56342	56836	2^{11}	54306	54568
2^{12}	57300	57857	2^{12}	55054	55304
2^{13}	58285	58879	2^{13}	55751	56019

*The peaks shifted by 0.73 eV.

kinds of solvents by using ESR. They used the Marcus-Hush theory[57] and the Bixon-Jortner theory[58], but could not reproduce the experimental results, since the electronic coupling strength is in the intermediate range. Fig.12 shows the numerical results. Calculations are made based on the one-dimensional model with use of the parameters taken from Ref.[106] except for the effective frequency ω, which is 1200 cm^{-1}, 950 cm^{-1}, 800 cm^{-1} for the three solvents, CH_3CN, DMF (dimethylformamide) and PrCN (butyronitrile), respectively. As can be seen, the experiment is nicely reproduced.

Applications of the present theory to charge transfer in organic semiconductors and organic molecules for solar cells are made by Nan *et al.*[107] and by Zhao and Liang[108] with use of quantum chemical electronic structure calculations. The numerical methods of Monte Carlo and umbrella sampling are employed to attack complex systems by Zhao *et al.* (see (d) of [60]). The determination of electronic structure parameters such as the reorganization energy λ and the coupling strength by quantum chemical calculations is not easy, unfortunately. Use of spectroscopic data is sometimes useful as is discussed by Nelsen *et al.*[109].
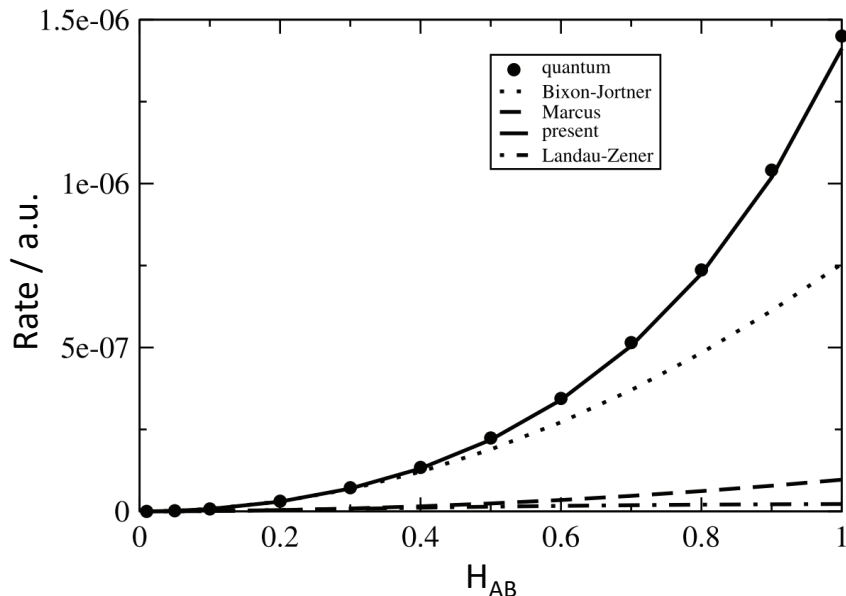
Figure 11: Electron transfer rate as a function of electronic coupling strength H_{AB} in the units of ω at low temperature $T = 0.3\omega$ and $\omega = 500$ cm^{-1}. Dot:quantum mechanical exact result, solid line:present NA-TST based on ZN theory, dot line:Bixon-Jortner theory, Dash line: Marcus theory, dash-dot:LZ formula.

4.4. Photodissociation of H_2SO_4

The isotopic imprint of sulfur bearing compounds is an important tool to understand the sulfur cycle of planetary atmosphere. Sulfur isotope analysis has been employed for many years to study the rise of oxygen on the Earth during the Archean period[110, 111, 112] and to understand the size, strength and emission features of stratospheric volcanic eruptions[113, 114]. Sulfur isotopes and non-mass dependent (NMD) fractionation effects have been applied to the study of meteorites[115] and to the study which links the deep sulfur cycle and the Martian atmosphere[116]. Recent experimental and theoretical studies[117] have presented the strong evidence of the involvement of intersystem crossings, i.e., potential surface crossings, as a potential origin of NMD fractionation for photoexcited (SO_2^*) species and for their significance for explaining the isotopic imprint of the geological record. Furthermore, a recent study[118] has reported the importance of potential surface crossings for the NMD effect during the photodissociation of SO.

Although the cyclic reactions have been proposed in several studies, the property of each reaction still has some ambiguity even in the reaction channel; for example, what kind of electronic states (excited/ground state or singlet/triplet state . . .) of product are correlated with the parent molecule in photodissociation process, etc. Concerning the sulfuric acid (H_2SO_4), the information of electronically excited states is still an open question, albeit the sulfuric acid is a representative one of the most
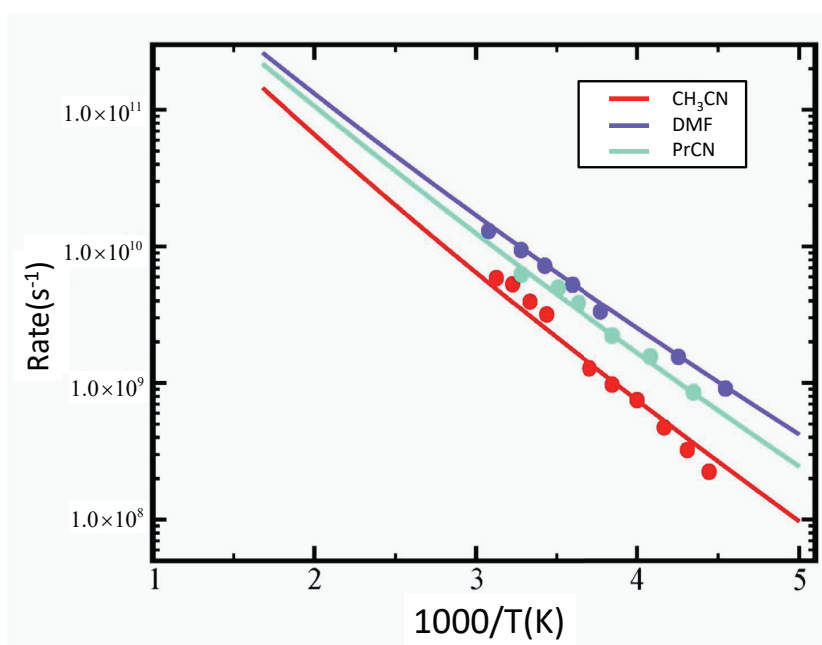
33

Figure 12: Arrhenius plot of electron transfer rate of 2,7-dinitronaphthalene in three kinds of solvents. Dots are experimental results of Nelsen *et al.*[106]. Lines are the results of present improved Marcus formula, Eq.(3. 30). Red line and symbol:CH_3CN, Green line and symbol:DMF, Purple line and small symbol:PrCN. The effective frequencies used are 1200 cm^{-1}, 950 cm^{-1}, 800 cm^{-1} for CH_3CN, DMF and PrCN, respectively. Reproduced from Ref.(c) of [60] by permission of World Scientific
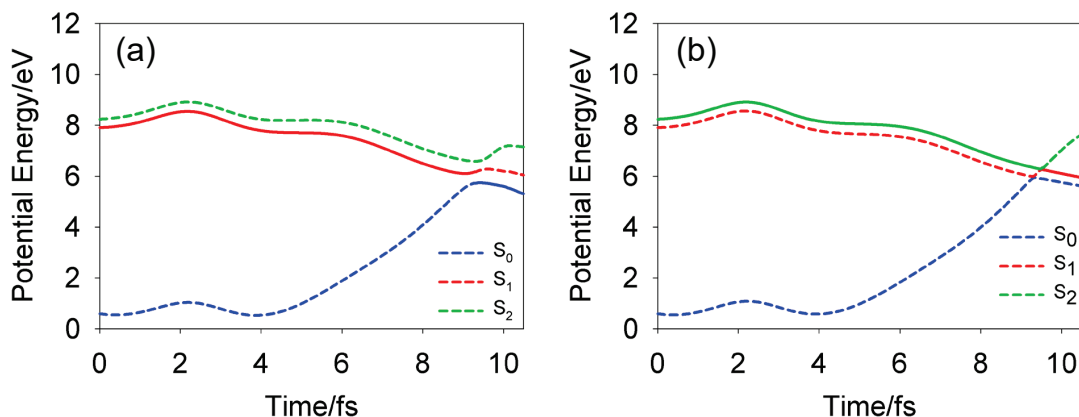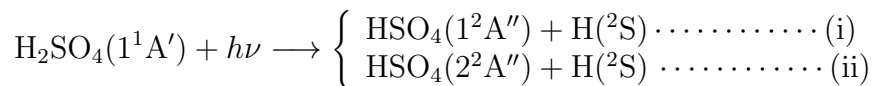
Figure 13: The time-evolution of the potential energy surfaces of a typical trajectory after photoexcitations of (a) $S_1 \leftarrow S_0$ and (b) $S_2 \leftarrow S_0$. The solid and dash lines represent the occupied state or unoccupied state, respectively.

oxidized sulfur.

In the present study, nonadiabatic *ab initio* molecular dynamics (*ab initio* MD) simulation was performed to explore the photodissociation dynamics of H_2SO_4 using the ZN-TSH method. The state-averaged CAS(8e, 8o)SCF/aug-cc-pVDZ is employed for the *ab initio* part. The photodissociation dynamics are carried out for the two excited states S_1 and S_2 for 20 fs after photoexcitation by using the on-the-fly *ab initio* method. If the bond length becomes twice larger than the bond length of the optimized geometry, it is assumed that the dissociation is over and the trajectory calculation is stopped. Fifteen and fourteen classical trajectories are propagated for S_1 and S_2 excited states, respectively. It is found that nonadiabatic transitions at potential surface crossings play crucial roles.

There are two dissociation channels, $S_0 \rightarrow S_1 \rightarrow S_0$ and $S_0 \rightarrow S_2 \rightarrow S_1$ (see Eqs.(i) and (ii) shown below).

$$H_2SO_4(1^1A') + h\nu \longrightarrow \begin{cases} HSO_4(1^2A'') + H(^2S) \cdots\cdots\cdots\cdots (i) \\ HSO_4(2^2A'') + H(^2S) \cdots\cdots\cdots\cdots (ii) \end{cases}$$

The time-profiles of the potential energy surfaces along a typical trajectory are shown in Fig.13. It is clearly seen that there occurs a nonadiabatic transtion at around 9.3 (9.7) fs for $S_1 \rightarrow S_0$ ($S_2 \rightarrow S_1$).

These reaction channels seem to be quite simple at first glance which provides the hydrogen atoms in the dissociation limit, but it is actually found that nonadiabatic
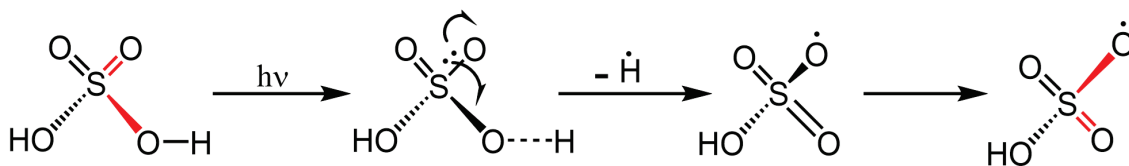
35

Figure 14: Bond alternation mechanism in the photolysis of H_2SO_4 via the first and second excited states.

transitions are involved in both channels[119]. Furthermore, the motion correlated with the nonadiabatic transitions is SO_2 antisymmetric vibration in sulfuric acid, namely, the bond alternation between single and double SO bonds occurs as shown in Fig.14. Note that the geometrical structures at these nonadiabatic transtions are very different from each other.
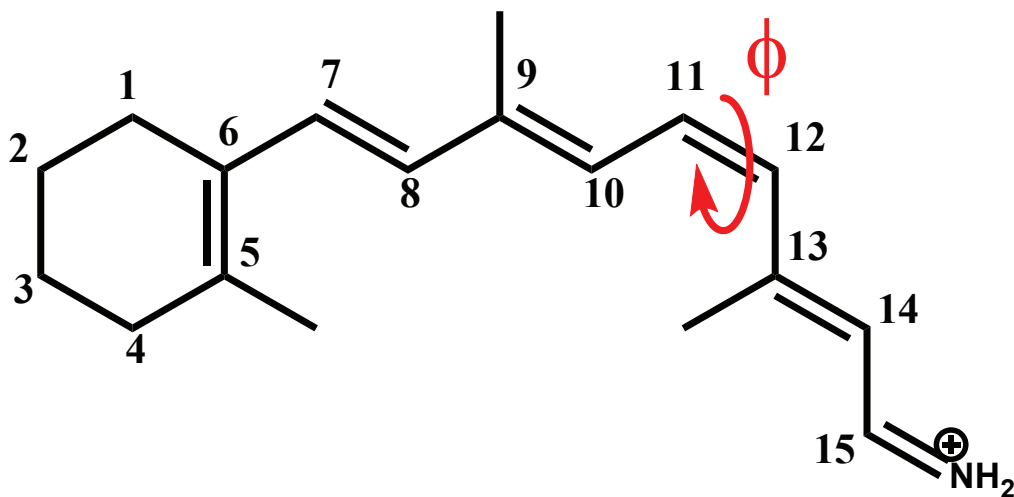
Figure 15: The (12π) model system of retinal used. The numbers attached show the positions of carbon atoms.

4.5. Nonadiabatic photoisomerization dynamics of protonated Schiff base retinal in vacuo

Retinal is a core molecule responsible for the vision of vertebrate animals including humans. The $cis{\to}trans$ isomerization causes electric impulse to be transmitted to the brain and recognized as light[120, 121]. Photoisomerization of protonated Schiff base retinal in vacuo is investigated with use of the *ab initio* ZN-TSH method[122]. In the case of polyatomic molecules it is not recommended to use analytical functions of potential energy surfaces, since it is a formidable task to prepare global *ab initio* potential functions in advance. Instead, it is recommended to use the so called on-the-fly *ab initio* method[123]. The model system of retinal molecule used here is the 12π system in which two methyl groups are removed from the Schiff base.

First, the isomerization of the 11-*cis* retinal is considered. This is composed of 45 atoms and presents a 129 dimensional problem (see Fig.15). The schematic energy diagram is shown in Fig.16. There are two conical intersections: one is in between all-*trans* form and 11-*cis* form and the other is in between 9-*cis* and 11-*cis*. The numbers mean the energies in kcal/mol measured from the all-*trans* ground state. The blue and red lines indicate the ground and excited states.

The molecule in the 11-*cis* form in the ground state is photoexcited and 98 classical trajectories are run. The initial geometry in the ground state is optimized by using the B3LYP method. The isomerization dynamics is investigated by using the generalized ZN-TSH method explained in Section 3.1 and potential energies are
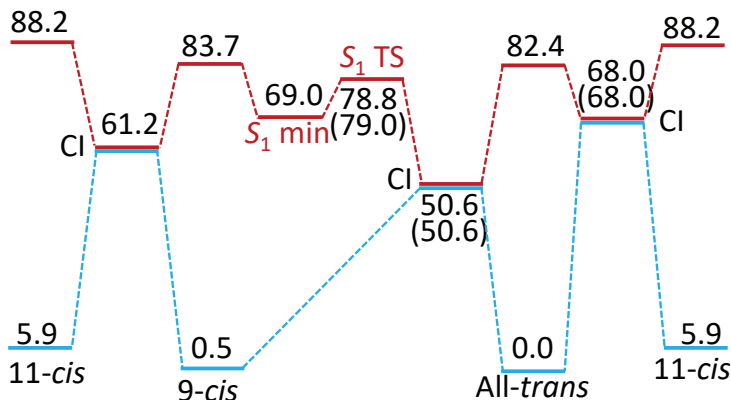
Figure 16: Energy diagram for *cis-trans* photoisomerization of retinal. The blue and red lines indicate the ground and excited states. Energy is in kcal/mol. At the conical intersections, numbers without/in parentheses indicate energy when the $C_8 - C_9 = C_{10} - C_{11}$ torsion is twisted in the clockwise/counterclockwise direction. CI = conical intersection, TS = transition state, min = minimum.

calculated on-the-fly by using the CASSCF(6,6) with the 6-31G basis set. Both Molpro 2006.1[124] and Gaussian 03[125] suits of *ab initio* programs are used.

The dynamics clarified is summarized as follows. The average time of nonadiabatic transition after photoexcitation is 125, 107 and 118 fs for all-*trans*, 9-*cis* and 11-*cis* state, respectively. The twisting bond is $C_{11} - C_{12}$ double bond. The bond length becomes longer like a single bond right after excitation, the bond twists to 60 - 100°, transition occurs to the ground state, then the bond goes back to double bond. After the transition the molecule stays in a certain intermediate state for a while and then finally stabilizes by going through a dynamical barrier which is not an ordinary potential barrier but a barrier due to the multidimensionality of the system. The time evolution of the dihedral angles is shown in Fig.17 for the case of all-*trans* formation. The angle $\phi(C_{11} - C_{12})$ [$\phi(C_9 - C_{10})$] decreases (increases) in all cases of all-*trans*, 9-*cis* and 11-*cis*, indicating the crankshaft motion.

The twist angle $|\phi|$ and its velocity $d|\phi|/dt$ at the hopping geometries are found to be $\phi| > 90°$ and $d|\phi|/dt > 0$ in the case of *trans* formation and $|\phi| < 70°$ and $d|\phi|/dt < 0$ in the case of *cis* formation. The two conical intersections are found to be equally accessed and the overall branching ratio turns out to be $\sim 1 : 1 : 2$ for all-*trans* : 9-*cis* : 11-*cis*. In reality the retinal molecule is embedded in rhodopsin protein environment and the 9-*cis* formation is blocked by the protein environment.
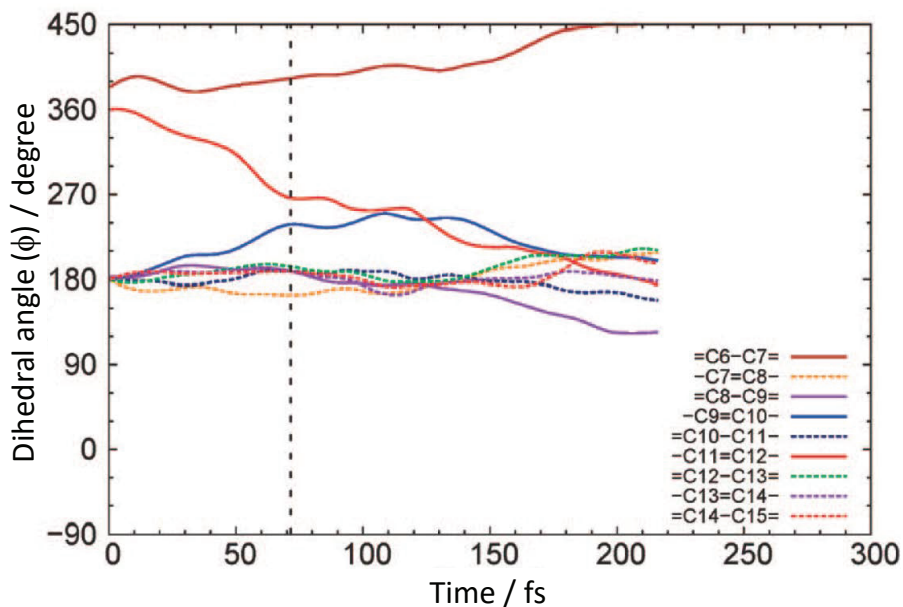
Figure 17: A typical time-evolution of dihedral angles of the backbone in the case of all-*trans* formation. The dashed line indicates the time of transition. Reproduced from Ref.[122] by permission of American Chemical Society (ACS).

If the 9-*cis* formation is counted as *trans* formation, the branching ratio becomes $\sim 1 : 1$ for *trans* : 11-*cis*. This agrees well with the experimental quantum yield in protein environment which is equal to 0.67.

Next, photoisomerization of 9-*cis* retinal in vacuo is investigated[126]. *Ab initio* quantum chemical calculations are carried out in the same way as above by using Molpro 2006.1 and Gaussian 03. The energy diagram is shown in Fig.16. A 10 kcal/mol potential barrier is found with the $C_8 - C_9 = C_{10} - C_{11}$ angle twisted $\sim 26°$ in the excited $S_1(^1\pi\pi^*)$ state. This was confirmed by more sophisticated quantum chemical computation. 71 classical trajectories are run with the time step 0.5 fs.

The overall photoisomerization process clarified by the present study is as follows. By the photoexcitation $S_0 \to S_1(^1\pi\pi^*)$ the bond length $R_9(C_9 = C_{10})$ stretches to a single bond (> 1.54 Å) and the torsion angle $\phi_9(C_9 = C_{10})$ twists by $\pm 30°$. The bond length R_9 (the angle ϕ_9) oscillates between single and double bond character (within $\pm 30°$) while being trapped in the S_1 potential well. When the potential barrier is surmounted, the crankshaft motion of ϕ_9 and ϕ_{11} is induced towards the conical intersection and finally the transition to the ground state occurs. In the crankshaft motion ϕ_9 and ϕ_{11} rotate clockwise and counterclockwise, respectively. The bond length R_9, being a single bond after surmounting the barrier, becomes a double bond (~ 1.34 Å). The angle ϕ_9, being greater than $70°$ before transition to all-*trans* form, becomes $0°$ or $180°$ finally on the ground state. Not like in the 11-*cis*

39

case, there is no two-step relaxation mechanism on the ground state. Because of the potential well and barrier in the excited state the $cis \rightarrow trans$ isomerization is slow and less efficient compared to the 11-cis case. This is not due to the so called pretwist[127]. The mechanism is intrinsic property of 9-cis retinal and not triggered by the protein environment. The branching ratio of all-$trans$ formation is 0.13 and it becomes 0.22 if the 11-cis is counted as $trans$ formation. This agrees well with the experimental quantum yield[128]. The X-ray structures are also consistent with the present results[129, 130]. The time spent from photoexcitation to the transition to the ground state is about 211, 292 and 284 fs for all-$trans$, 11-cis and 9-cis formation, respectively. This is $2 \sim 3$ times longer than in the case of 11-cis. Human evolved to choose the faster 11-cis retinal in rhodopsin for visual recognition.

In the above treatments the environment protein is totally neglected. In reality, the 11-cis retinal is embedded in rhodopsin and 9-cis retinal is embedded in isorhodopsin. In order to take into account the effects of environment protein we can combine the QM/MM and the ZN-TSH methods. This will be discussed in Section 4.7.

4.6. Photo-chemical dynamics of indolylmaleimide derivatives

Compounds with highly selective fluorescence attract significant interest because of various applications in chemical, environmental and biological sciences. It is an important research subject to design probes with controlled fluorescence yield and selective ON-OFF switching depending on the variations of environmental conditions. Here we investigate photo-chemical dynamics of indolylmaleimide derivatives, molecular structures of which are shown in Fig.18 [131]. Indole derivatives which attract much interest in biology are well known as fluorescent compounds. The fluorescence process is governed by the intra-molecular charge transfer in which indole and maleimide play roles of electron donor and acceptor, respectively.

There are following three anionic species which exist in solution (see Fig.18), (i) monovalent anion with a deprotonated indole NH group ($\mathbf{IM}^{-'}$), (ii) monovalent anion with a deprotonated maleimide NH group ($\mathbf{IM}^{-''}$) and (iii) divalent anion with doubly deprotonated indole and maleimide NH groups ($\mathbf{IM}^{2-}$). The photo-absorption maxima in acetonitrile solution are experimentally known to appear at 270 nm and 396 nm, but it is still unknown which species governs the photoemission process. In order to clarify this, it is crucial to investigate the deactivation processes due to nonadiabatic transitions by carrying out on-the-fly nonadiabatic $ab\ initio$ molecular dynamics computations.

The $ab\ initio$ quantum chemical calculations are carried out by using the state-averaged 6-electron 5-orbital complete active space self-consistent field (CAS(6e,5o)-SCF) scheme with Dunning's cc-pVDZ basis set. The package Molpro 2006.1 and 2008.1 are used [132]. The initial molecular coordinates and momenta are generated by random numbers subject to the Wigner distribution, which reflects the vibrational
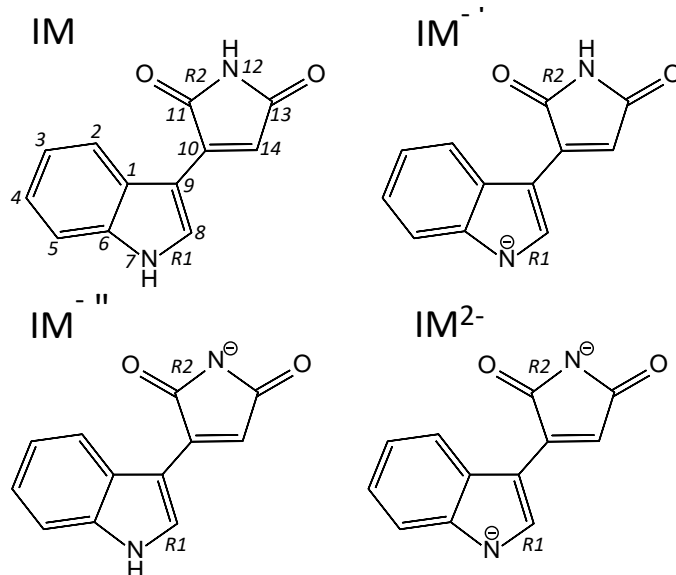
40

Figure 18: Molecular structure of indolylmaleimides; the numbers attached to the structures show the positions of carbons and nitrogens.

wave function at the zero-point energy. The time step of the time-evolution of classical trajectories is 0.25 fs and the trajectories are propagated until 60 fs. The dynamics calculations are performed by using the ZN-TSH method. Table 3 shows the oscillator strengths at the minimum energy geometry of the S_0 and S_1 states.

As is clearly seen, the $\mathbf{IM}^{-''}$ molecule cannot be the candidate of the photoemission species, because the $S_1 \leftarrow S_0$ and $S_2 \leftarrow S_0$ photoabsorption transitions are almost forbidden. Thus, the dynamics of $\mathbf{IM}^{-'}$ and $\mathbf{IM}^{2-}$ are mainly investigated here. The primary electronic configurations for both S_1 and S_2 states of $\mathbf{IM}^{-'}$ are mixed excitations of $(54a)^1 \rightarrow (56a)^1$ and $(55a)^1 \rightarrow (56a)^1$. The configuration of the S_1 state of $\mathbf{IM}^{2-}$ is $(55a)^1 \rightarrow (56a)^1$ and that of the S_2 state is $(55a)^1 \rightarrow (57a)^1$. The $(55a)^1 \rightarrow (56a)^1$ or $(54a)^1 \rightarrow (56a)^1$ excitation of $\mathbf{IM}^{-'}$ and $(55a)^1 \rightarrow (56a)^1$ of $\mathbf{IM}^{2-}$ correspond to the electron transfer from $\pi-$MO localized on the deprotonated indole moiety to π^*-MO localized on the maleimide moiety.

Figure 19 shows the energy diagram for S_0, S_1 and S_2 states of $\mathbf{IM}^{-'}$ and $\mathbf{IM}^{2-}$. Photoemission from the S_1 state is almost forbidden at the S_1 minimum energy structure for both $\mathbf{IM}^{-''}$ and $\mathbf{IM}^{2-}$, as can be seen from Table 3. On the other hand, Fig.19 indicates that the nonadiabatic transitions through conical intersections seem to be possible for both transitions $S_1 \rightarrow S_0$ and $S_2 \rightarrow S_1$. This means that it is not easy to determine which species, $\mathbf{IM}^{-'}$ or $\mathbf{IM}^{2-}$, is the one to emit photons without carrying out dynamics calculations. Total numbers of classical trajectories in the case of vertical excitation to S_1 for $\mathbf{IM}^{-'}$ and $\mathbf{IM}^{2-}$ are 40 and 20, while the numbers of trajectories in the case of excitation to S_2 are 34 and 18, respectively.

Table 3: Oscillator strengths at the minimum energy geometry in the S_0 and S_1 states.

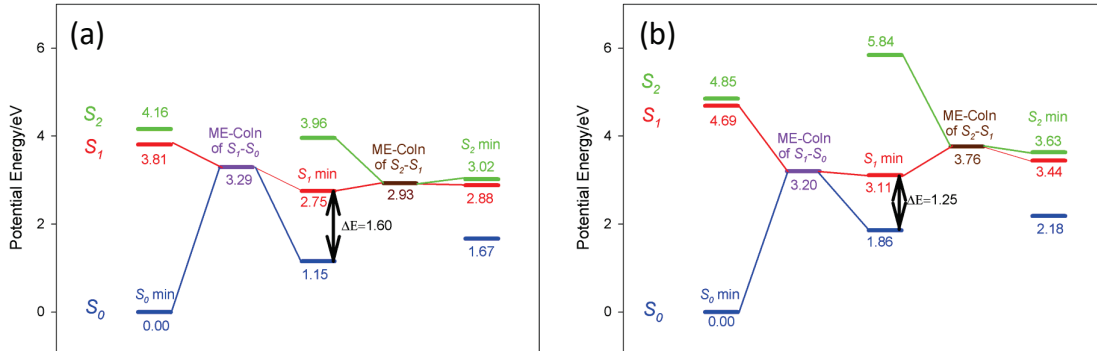|	Oscillator strength	
	S_0 min	S_1 min
(a) $\mathbf{IM}^{-'}$		
S_0-S_1	0.48	0.01
S_0-S_2	0.51	0.70
(b) $\mathbf{IM}^{-''}$		
S_0-S_1	0.02	0.01
S_0-S_2	0.01	<0.01
(c) $\mathbf{IM}^{2-}$		
S_0-S_1	0.50	<0.01
S_0-S_2	0.40	0.01

Figure 19: Relative energies for the S_0, S_1, S_2 states and minimum energy conical intersections (ME-CoIns) between S_1 and S_0 and between S_2 and S_1 for (a) $\mathbf{IM}^{-'}$ and (b) $\mathbf{IM}^{2-}$ where the potential energies at the most stable structures in S_0 are set to be zero.
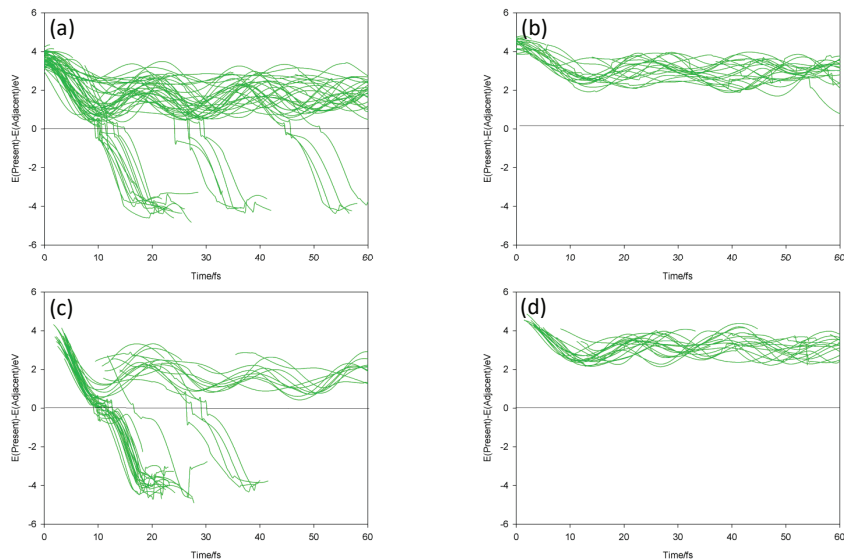
Figure 20: Time-evolution of energy difference between S_1 and S_0 for each trajectory of (a)$\mathbf{IM}^{-'}$ and (b) $\mathbf{IM}^{2-}$ after excitation to S_1 and (c)$\mathbf{IM}^{-'}$ and (d) $\mathbf{IM}^{2-}$ after excitation to S_2, respectively.

The dynamics computations are stopped, when trajectories relax to the S_0 state.

Figure 20 show time-evolutions of the energy differences between S_1 and S_0 states for all trajectories after the excitation $S_1 \leftarrow S_0$ [(a) and (b)] and $S_2 \leftarrow S_0$ [(c) and (d)] for $\mathbf{IM}^{-'}$ [(a) and (c)] and $\mathbf{IM}^{2-}$ [(b) and (d)]. The energy difference is taken to be positive (negative) when the trajectory is on the S_1 (S_0) state. Fig.20(a) shows that the nonadiabatic transition from S_1 to S_0 in the case of $\mathbf{IM}^{-'}$ takes place with 60 percent probability. The average period of this nonadiabatic transition after excitation is about 36.19 fs. Fig.20 (c) also shows that 76.5% of the excited state trajectories are deactivated to S_0 within 60 fs due to the two sequential nonadiabatic transitions of $S_2 \to S_1$ and $S_1 \to S_0$. The average period of the nonadiabatic transition from S_1 to S_0 is about 26.16 fs. On the other hand, Figs.20 (b) and (d) indicate that in the case of $\mathbf{IM}^{2-}$ nonadiabatic transitions between S_1 and S_0 do not occur at all, although the transition from S_2 to S_1 occurs through the corresponding conical intersection as shown in Fig.19 (b). This means that $\mathbf{IM}^{2-}$ does not decay to S_0 non-radiatively and stays on the S_1 state, irrespective of the excitation process of $S_1 \leftarrow S_0$ or $S_2 \leftarrow S_0$. This is the most important finding of the present work and suggests that $\mathbf{IM}^{2-}$ would be the species to contribute to the photoemission. The two nonadiabatic coupling vectors in the case of $\mathbf{IM}^{-'}$ for both S_2-S_1 and S_1-S_0 transitions have large components on the five-membered ring of the indole moiety. In contrast in the case of transition S_2-S_1 of $\mathbf{IM}^{2-}$, the vector has the main components around the maleimide moiety. The stretching and shrinking motions of each ring

are the driving force for the actual nonadiabatic transitions. The bond length R_1 of N(7)-C(8) and R_2 of C(11)-N(12) stretch to 1.4 Å immediately after photoexcitation, which corresponds to the positions of the S_2-S_1 conical intersections. The $S_1 \rightarrow S_0$ transition in the case of $\mathbf{IM}^{-'}$ occurs due to R_1 stretching.

4.7. Photo-isomerization of retinal in opsin environment

Rhodopsin (Rh) is the photosensitive chemical in the outer segment of rod-like cells in the light-sensing structure of the eye, i.e., retina. The 11-*cis* retinal chromophore in Rh changes to all-*trans* form upon exposure to light and bathorodopsin (bathoRh) is produced in the Rh photocycle. Isorodopsin (isoRh) is an analogue of Rh that contains a 9-*cis* retinal chromophore embedded in the same opsin environment. The 9-*cis* retinal is also converted to all-*trans* form, producing bathoRh in the same way as in the Rh case. In spite of structural similarity and the same product formation, Rh and isoRh show quite different rates and efficiencies of photoisomerization. Isomerization of 11-*cis* (9-*cis*) retinal in Rh (isoRh) to all-*trans* essentially completes in about 200 fs (600 fs)[133]. The isomerization quantum yield in Rh (isoRh) is reported to be 0.65 - 0.67 (0.22)[134, 135, 128]. A comparative study of the isomerization of Rh and isoRh is very attractive because of the big differences in reaction time scale and quantum yield despite a small structure difference.

With use of the Landau-Zener formula Schoenlei *et al.* suggested that the slower reaction time and lower quantum yield in isoRh are due to slower motion along the reaction coordinate in the curve crossing region (see (c) of Ref.[133]). From the X-ray structure analysis Nakamichi *et al.* proposed that the significant pretwist of the twist angle ϕ_9 of $C_8 - C_9 - C_{10} - C_{11}$ is responsible for Rh's highly efficient isomerization[127]. In order to clarify the isomerization dynamics of Rh and isoRh we have employed the ZN-QM/MM-TSH method, in which the QM/MM method is combined with the ZN-TSH method as explained in Section 3.4.1[136]. The QM part, namely, quantum chemical calculation is performed for the retinal, the same as that in the treatment in vacuo, and the opsin environment is treated by MM (molecular mechanics) described by AMBER force field parm96.dat[137] embedded in Gaussian09[140]. The quantum chemical calculations are carried out with the level of CASSCF(6,6) with the 6-31G basis set. The number of atoms taken into account for Rh (isoRh) is 5591 (5692). A total of 162 classical trajectories are computed for both Rh and isoRh with 0.5 fs time step. It took typically 7 weeks for one trajectory on Intel Core machine with a clock of 2.66 GHz. The quantum yield or reaction probability, Φ, computed with one standard deviation for the mean is calculated by the following formula[138],

$$\Phi = \frac{N_R}{N}\Big(1 \pm \sqrt{\frac{1}{N-1}(\frac{N}{N_R}-1)}\Big), \qquad (4.\ 1)$$

where N is the total number of trajectories and N_R is the number of reactive trajectories.
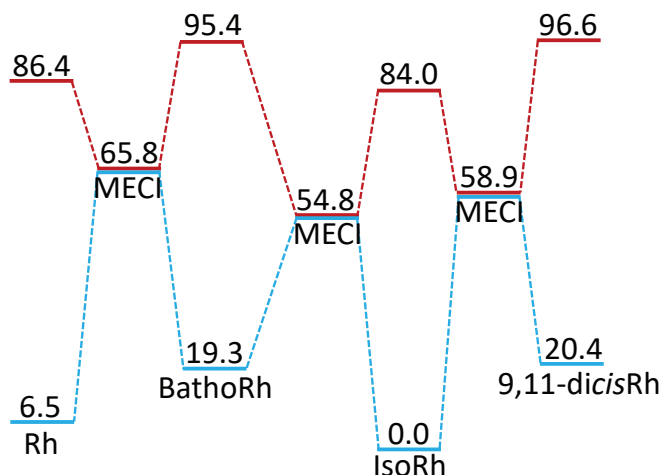
Figure 21: Energy diagram for the $cis - trans$ isomerization of Rh and isoRh. Energy is in kcalmol^{-1}. The blue and red lines indicate the ground and excited states, respectively. MECI = minimum energy conical intersection. The energy for an MECI is the average of the energies of S_1 and S_0.

In this study, two rotation centers ($-C_9 = C_{10}-$ and $-C_{11} = C_{12}-$) are closely monitored and the isomers are classified according to these torsion angles, giving rise to the four isomeric species: Rh, isoRh, bathoRh and 9,11-di-cis isomers. Fig.21 shows the energy diagram for the ground (S_0) and the first excited state (S_1) spanned by these isomers. The relative ground-state energies of the isomers are different from those in vacuo[126]. The direction and the relative magnitude of the pretwist is in good agreement with the X-ray observation[127]. The angle ϕ_9 and ϕ_{11} deviate rather largely from the perfect $trans$ configuration at the bathoRh equilibrium configuration, which is also in good agreement with X-ray crystallography results[139]. On the other hand, the present excitation energies ranging from 76 to 84 kcal/mol are larger than the experimental measurements (53 - 59 kcal/mol). Nevertheless, the relative order of the vertical excitation energies is qualitatively reproduced. This qualitative reproduction should be sufficient for the present purpose. The small potential barrier found in our previous calculation of isoRh in vacuo[126] is not found in the present calculation. The reason for this is not clear at this stage, unfortunately. Probably, much higher level of quantum chemical calculations would be needed to clarify this and that is currently beyond our scope. The ground and excited state surfaces are connected by conical intersections (CI) which exist on the half way between cis and $trans$ forms along each twist angle. In all cases the double bond in the active torsion coordinate stretches to a single bond at minimum energy CIs.

45

In our previous calculations we found a CI that directly connects 9-*cis* and 11-*cis*, but that disappears when the opsin environment is taken into account. Overall, the calculated results are in qualitative agreement with the experimental measurements, and thus we may say that the present calculations well simulate the dynamics of the systems.

The calculated quantum yields are 0.52 and 0.31 for Rh and isoRh, respectively. The corresponding experimental values are 0.65 and 0.22, as mentioned before[135, 128]. The slight overestimation of the isoRh quantum yield may be due to the underestimation of the disturbance by the opsin environment and irreproducibility of the S_1 barrier. Photoexcitation of Rh only leads to bathoRh and the reactant, and generation of isoRh is totally blocked by the opsin environment. Thus, as mentioned before, the trajectories that lead to 9-*cis* isomer without the opsin environment are actually blocked away to generate all-*trans* bathoRh instead. It is also found that the opsin environment totally blocks simultaneous twisting of ϕ_9 and ϕ_{11} for Rh as well as isoRh, while the twist in the opposite direction of ϕ_9 and ϕ_{11} can be seen in all cases. Photoexcitation of isoRh yields a small amount of 9,11-di-*cis* product (4%) in addition to bathoRh, whereas Rh provides the bathoRh alone. Thus, the rigorous selectivity of Rh production would be another biological reason for living creatures to choose Rh rather than isoRh. As shown in Fig.22 for the time-evolution of classical trajectories, the population of bathoRh reaches maximum at 187 and 344 fs for Rh and isoRh, respectively. The experimentally observed periods (200 and 600 fs) are reasonably reproduced with a slight underestimation. This underestimation would be mainly due to the overestimation of excitation energies and the underestimation in the case of isoRh may be due to the lack of a potential barrier in the excited state. The fact that the dynamics in the case of Rh is fast and straightforward is responsible for coherence, higher quantum yield and shorter reaction time. In the case of isoRh, on the other hand, the back-and-forth and complicated dynamics leads to slower and less efficient isomerization. In both Rh and isoRh cases all trajectories exhibit "wring-a-wet-towel" motion of ϕ_{11} and ϕ_9. For all trajectories in Rh as well as most of trajectories in isoRh, the active angle (ϕ_{11} in the case of Rh and ϕ_9 in the case of isoRh) twists in the counterclockwise direction and the associate angle (ϕ_9 in the case of Rh and ϕ_{11} in the case of isoRh) twists in the clockwise direction. Only exception is a small portion of isoRh (13%), where the active angle twists in the clockwise direction and associate angle twists in the couterclockwise direction. All the Rh trajectories go through only one CI with $\phi_{11} \sim -90°$ and slightly clockwise-twisted ϕ_9 which leads to bathoRh. The relaxation of excited isoRh, on the other hand, goes through two CIs, one leading to bathoRh and the other leading to 9,11-di-*cis*. As mentioned before there is no CI directly connecting Rh and isoRh.

In summary, the Rh protein environment ensures that the photoisomerization proceeds in the right direction and optimizes the all-*trans* product; whereas the tendency to photoisomerize upon absorption of photon is intrinsic to the central chromophore itself by Nature's design. Also the isoRh formation from Rh is totally
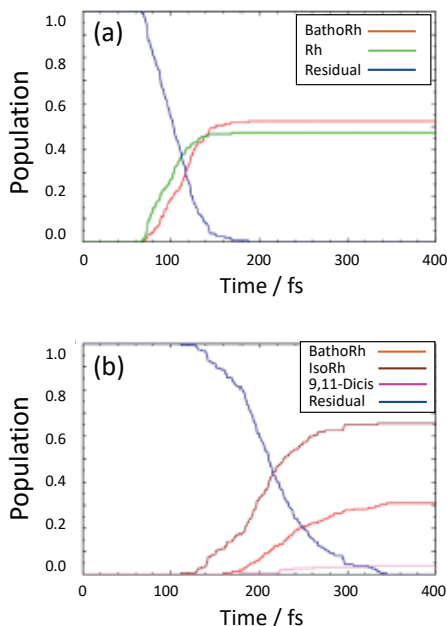
Figure 22: Time evolution of population in the case of (a) Rh and (b) isoRh. Population is counted only after the product region is reached on the ground state. Reproduced from Ref.[126] by permission of ACS.

blocked and vice versa. Furthermore, the opsin makes transitions to take place near the CIs. The ZN-QM/MM-TSH scheme is a promising approach for a wide range of applications. Wider range of QM part with higher level of quantum chemical calculations would surely yield much better results.

4.8. Photo-isomerization of (z)-penta-2,4-dieniminium cation (benchmark system) in methanol solution

In order to demonstrate the power of the PME-ONIOM-MD method, namely the ZN-PME-TSH method, we have investigated the title process[96]. (Z)-penta-2,4-dieniminium cation (protonated Schiff base, PSB3) is the minimal model based on 13-*cis* isomer of 11-*cis*-retinal protonated Schiff base (PSB11), as shown in Fig.23.

First, the ordinary classical MD simulation was performed to determine the initial molecular coordinates and box size of the central layer under NPT condition for 10 ns at 1.0 atm and 300 K. The solute molecule is embedded in 36 methanol molecules and one chloride ion is added to neutralize the unit cell. The charges of atoms in the unit cell are taken into account in the QM calculation by the electrostatic embedding scheme, and the external charge effect is handled classically by the PME scheme. In the MM calculation, the force field parameters are taken from general AMBER force field (GAFF) and the charges of atoms are given by restricted electrostatic potential charge method. These parameters are generated with Leap
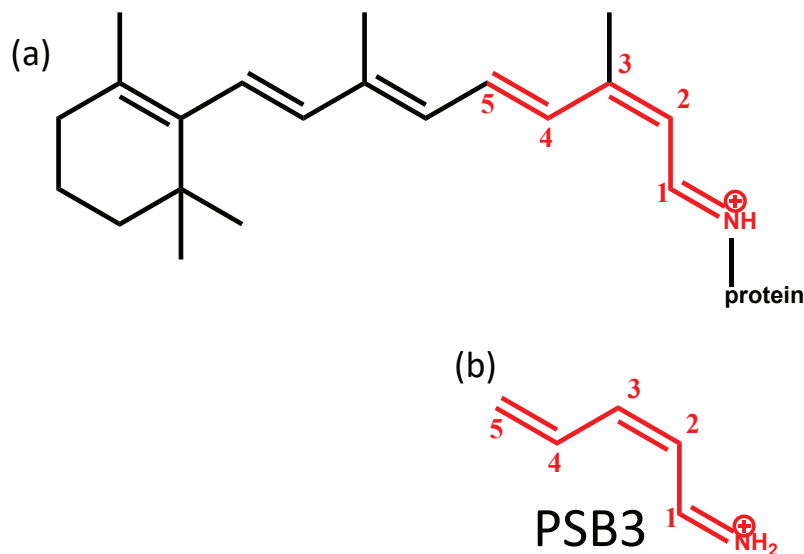
47

Figure 23: The molecular structures of (a) 13-*cis* isomer of PSB11 and (b) PSB3.

and ANTECHAMBER programs, which are also available in AMBER9. The size of the unit cell employed is 2518 Å^3, and the density for solute and solvent is 0.7606 g/cm^3, while the concentration of PSB in solution is 0.0542 g/cm^3.

For the *ab initio* quantum chemical calculations the state-averaged CASSCF method with use of the MIDI4* basis set[141] in the package MOLPRO2012.1[142] is used. Other *ab initio* methods such as MS-MR-CASPT2/cc-pVDZ, SA-CASSCF/cc-pVDZ and MRCI/cc-pVDZ are also used to check the validity of the present approach and the SA-CASSCF/MIDI4* was found to be reasonable for the present purpose. In stead of PME the minimum-image (MI) convention is also used for comparison. The total number of classical trajectories is 50 in each case and the time step is 0.5 fs. All the trajectories are propagated until the isomerization is over.

It should be noted that there are two isomerization channels in solution (see Fig.24): (i) through the conical intersection with the central C=C double bond twisting (channel 1) and (ii) through the conical intersection with the terminal C=N double bond twisting (channel 2). The channel 2, which does not appear in gas phase[122], is revealed to appear in solution, since the solvent stabilizes the relevant conical intersection and this CoIn becomes energetically accessible[143].

Figures 25 show time-evolutions of the trajectory population for the three channels: (i)S_1 state, (ii)S_0 state via the C=C twisting isomerization and (iii)S_0 state via the C=N twisting isomerization.

The S_1 state lifetimes mainly attributed to the channel 1 (C=C isomerization) and the channel 2 (C=N isomerization) are 3.483 ps and 81.74 fs, respectively in
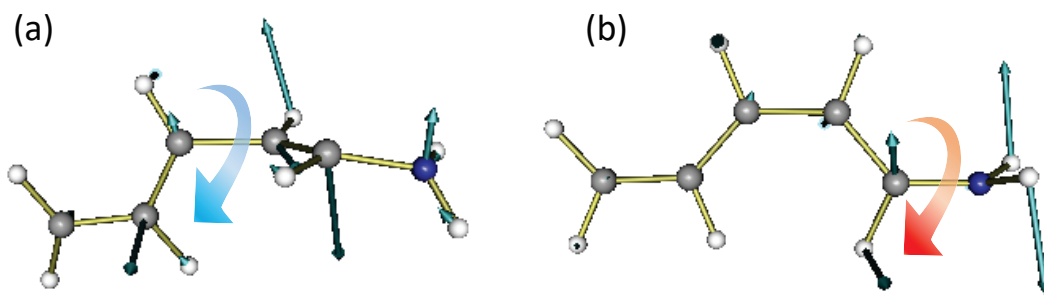
Figure 24: The molecular structures and nonadiabatic coupling vectors at the conical intersections of the two typical trajectories. (a) C=C twisting motion and (b) C=N inner rotation.
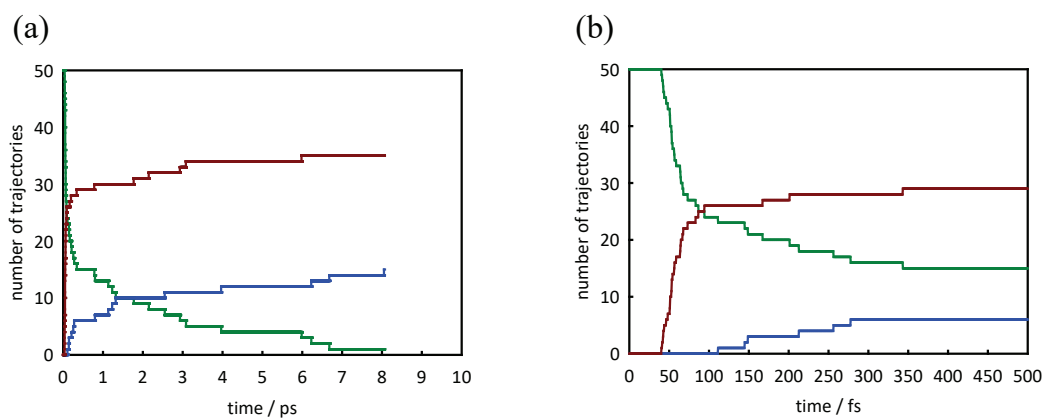

Figure 25: The population of all trajectories as a function of evolution-time; trajectories which stay in S_1 are green. Those having hopped to S_0 with C=C isomerization are blue. Those with C=N inner rotation are brown. (a) and (b) show the whole profile and the first 500 fs.

Table 4: Lifetime by PME-ONIOM-MD and MI-ONIOM-MD simulations

Theoretical approach	Channel-1 (C=C)	Channel-2 (C=N)
PME/SA-CASSCF/MIDI4*	3.434 ps	81.74 fs
MI/SA-CASSCF/MIDI4*	0.4642 ps	91.43 fs

the case of PME-ONIOM-MD/SA-CASSCF/MIDI4* method, as is shown in Table 4. The MI-ONIOM-MD/SA-CASSCF/MIDI4* calculations are also performed and the corresponding life times are shown in Table 4. The life time 91.43 fs of the inner rotation (channel 2) is similar to that of PME case, but the life time 0.4642 ps of C=C isomerization (channel 1) is much shorter than that of PME. Actually, the PME result is in accordance with the experimental finding[144] that there are two reaction paths with 90 fs and 3.5 ps lifetimes. This is one of the most important results of the present calculations. The solvent charge clearly affects the behavior of the nonadiabatic phenomenon of the C=C isomerization, since this isomerization is characterized by charge transfer. This effect is nicely reproduced by the present PME method with the long range interactions properly taken into account by the periodic boundary condition.

A typical time-evolution of the bond lengths and its dihedral angles is analyzed in the two channels. In the case of channel 1, the bond length gradually stretches to 1.45 Å by about 2400 fs and the dihedral angle is twisted by about -60 degrees. This is due to the bond character change from sp^2 hybridization to sp^3 by losing the double bond character. This is in accordance with the charge transfer mechanism mentioned above. In the case of channel 2 (C=N twisting) the bond length of C=N remains at 1.4 Å up to 75 fs and the dihedral angle rapidly twists by more than -90 degrees.

Finally, it is noted that the life times obtained by PME-ONIOM-MD/MS-MR-CASPT2/MIDI4* are 135.9 and 49.12 fs for channels 1 and 2, respectively. These do not agree with the experimental finding, especially the time scale of channel 1 is quite different. This is due to the large bore funnel of conical intersection created by MS-MR-CASPT2.
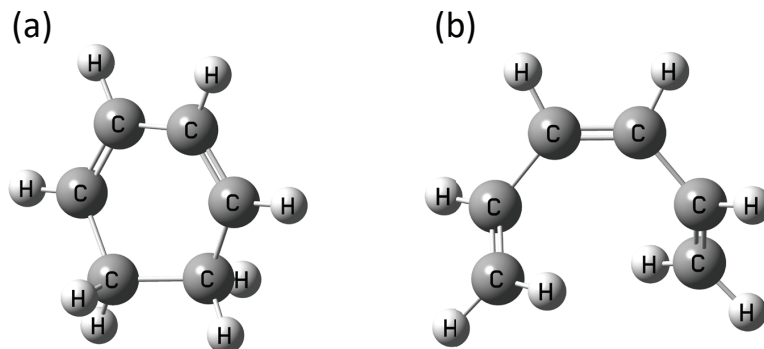
Figure 26: The molecular structures, (a) 1,3-cyclohexadiene (CHD) and (b) 1,3,5-*cis*-hexatriene (HT).

4.9. Photo-isomerization reaction between 1,3-cyclohexatriene and 1,3,5-*cis*-hexatriene in vacuo and solution

The reversible structural transformation of photochromic molecules has fascinated us over the 20th century. The applications are diversifying into various fields of photochemistry, material science and biochemistry in the 21st century. Some of photochromic systems are based on chemical compounds containing the Kekul-type structure defined by six-carbon skeleton. The photoisomerization between 1,3-cyclohexadiene (CHD) and 1,3,5-*cis*-hexatriene (HT) structures is the simplest system to represent the feature (see Fig.26) compared to diarylethenes, fulgides and vitamin D [145]-[148]. This prototype photoreaction has also attracted a great deal of interest as a simple model in both theoretical [149]-[163] and experimental [167] -[187] studies. Kosma *et al.* experimentally observed the CHD/HT isomerization in gas-phase by the time-resolved photoelectron/mass spectroscopy[185]. CHD was photoexcited to S_1 by the ultrashort third harmonic pulse at 270 nm. They reported that molecular wavepacket passes through the conical intersection (CoIn) of $1^1B/2^1A$ (S_1/S_2) at 56 fs after photoexcitation, and then the wavepacket is deactivated into S_0 through the CoIn of $2^1A/1^1A$ (S_0/S_1) at 136 fs. Pullen *et al.* also made observations of this photoisomerization and the subsequent energy dispersion process in cyclohexane solution by using two-color transient absorption kinetic measurements and novel time-resolved absorption spectroscopy at the 260 - 300 nm[173, 174]. Their measurement uncovered that the sub-picosecond photoproduct formation of CHD

or HT occurs on the time-scale of 250 fs, and then the isomerization to other structural isomers of HT, *i.e.* *cZt*-HT and *tZt*-HT, happens in the electronic ground state because of the energy dispersion after the ultra-fast photoproduct formation. This energy stabilization of HT isomers in S_0 was observed on the time-scale of 1 - 5 ps. The product ratio of CHD:HT in cyclohexane solvent was reported as 60:40[175]. The CHD/HT photoisomerization in ethanol solvent was also investigated by transient absorption spectroscopy in the wavelength range between 255 and 450 nm by Lochbrunner *et al.* Their study in ethanol solvent suggested that the photoproduct formation of CHD or HT occurs within 300 fs[176].

On the other hand, Tamura *et al.* studied quantum dynamics of this reaction by using the wavepacket propagation method on a two-dimensional potential energy surface[160]. The branching ratio between CHD and HT was found to be 50:50 in their model. The time duration of the first decay 1^1B-2^1A is approximately 15 - 25 fs, and then the molecular wavepacket goes through the next CoIn of S_0/S_1 at 130 fs. Hofmann and de Vivie-Riedle also performed the wavepacket dynamics using the effective Hamiltonian based on the three-dimensional model[155]. The correlation between the theoretical CHD:HT ratios and locations of CoIn was discussed by them. Although some other theoretical studies have also been reported so far, any simulation has not yet been carried out with all degrees of freedom taken into account. In many cases, in order to reduce the computational cost the effective Hamiltonian in the framework of the reduced dimensional model has been employed. Usually, the ring opening degree of CHD and the dihedral angle are taken into account.

In the present study, nonadiabatic *ab initio* molecular dynamics (*ab initio* MD) simulation is performed to explore the CHD/HT isomerization dynamics initiated by the photoexcitation of CHD to the S_1 and S_2 states[164]. Particularly, the solvation effects in hexane and ethanol solvents are investigated by the ZN-PME-TSH hybrid method (see Fig.27)[164, 165, 166].

The MS-MR-CAS(8e,8o)PT2/cc-pVDZ is employed for the QM part. The simulation is performed for 2 ps, because the experimental time-resolved measurement of this isomerization has reported the picosecond-order lifetime. Time-profiles of QM part (CHD) potential energy in solution phases show smaller fluctuation than in-vacuo case (see Fig.28). This means that the molecular motions of CHD solute are confined by the solvent molecules.

The radial distribution function (RDF) is numerically analyzed with respect to solute-solvent interaction. As shown in Fig.29, ethanol solvent (red line) has stronger peaks around 5 Å than hexane solvent, which means that there is a strong cage effect in ethanol solvent. The cage effect would appear because of the induced dipole moment of CHD in ethanol solvent; the dipole moment in the S_2 state is 1.02 Debye [166]. Since the hydorgen-bond network is constructed by hydroxy group of ethanol solvent, the weakly charged CHD is surrounded by the hydorgen-bond network in the electronic excited state. On the other hand, hexane solvent (black line) shows an almost uniform distribution. As Dias *et al.* pointed out[188], the
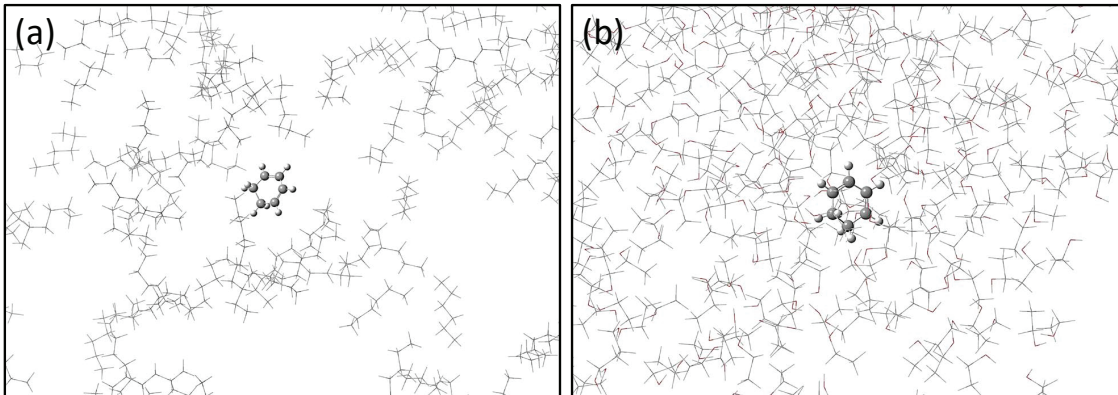
Figure 27: CHD molecule (indicated by ball and stick model) surrounded by 304 solvent molecules, (a) hexane and (b) ethanol solvents.

Table 5: The product branching ratio (CHD:HT) determined by nonadiabatic *ab initio* MD simulations for photoexcitations to S_1 and S_2 in each solvent.

Photoexcitation	In hexane	In ethanol	In vacuo
$S_1 \leftarrow S_0$	40:60	80:20	60:40
$S_2 \leftarrow S_0$	30:70	60:40	70:30

RDF of hexane solvent has a similar uniform distribution, albeit their simulations are different from our approach. This uniform distribution is generally attributed to the high flexibility of liquid structure. The strong affinity between hexane and CHD is due to nonpolar solutions, which caused the high flexibility between solute and solvent. The efficiency of the photochromic conversion of CHD to HT is evaluated at both S_1- and S_2-excitations in two different types of solvents, ethanol and hexane. The CHD:HT branching ratios of the products are listed in Table 5. The solvent-dependent branching ratios can be explained also by the flexibility of liquid structure and demonstrate the power of the present method.
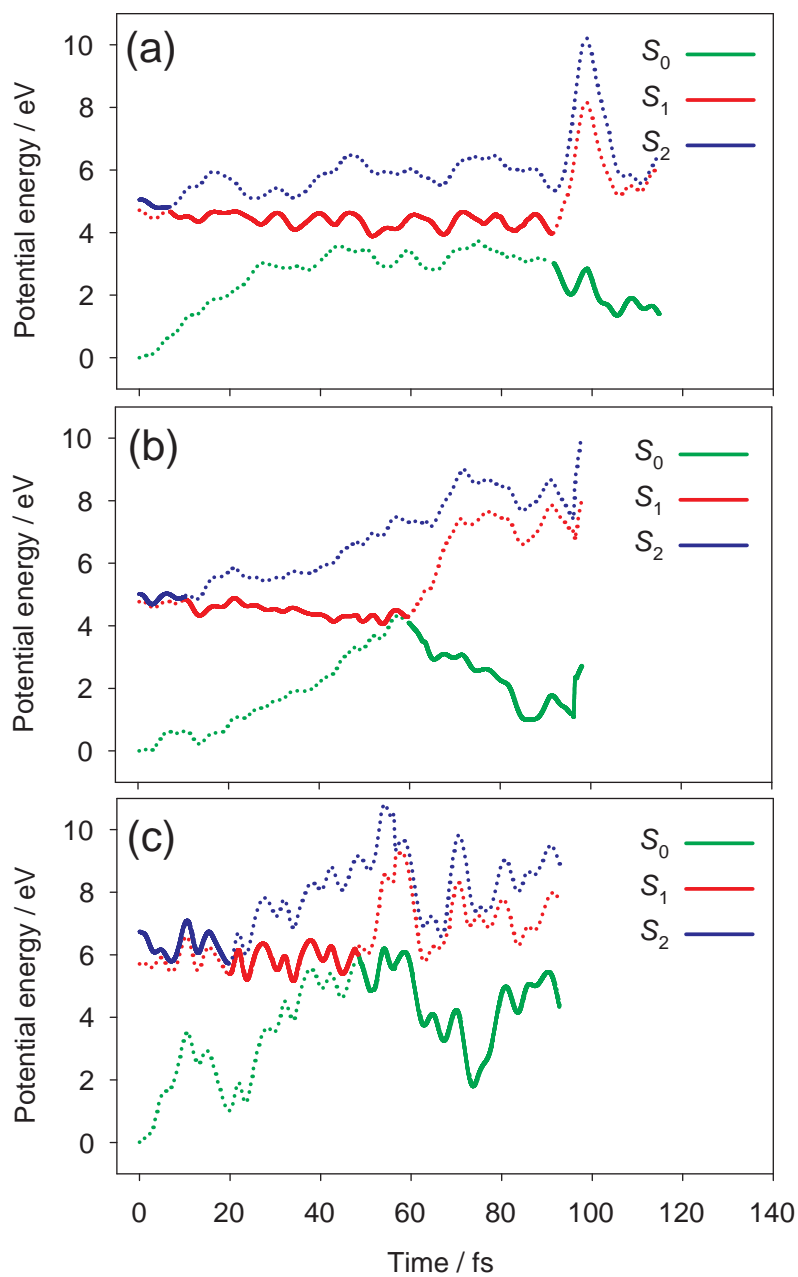
Figure 28: A typical time-evolution of potential energies of QM part in (a) hexane, (b) ethanol and (c) vacuum after photoexcitation to S_1.
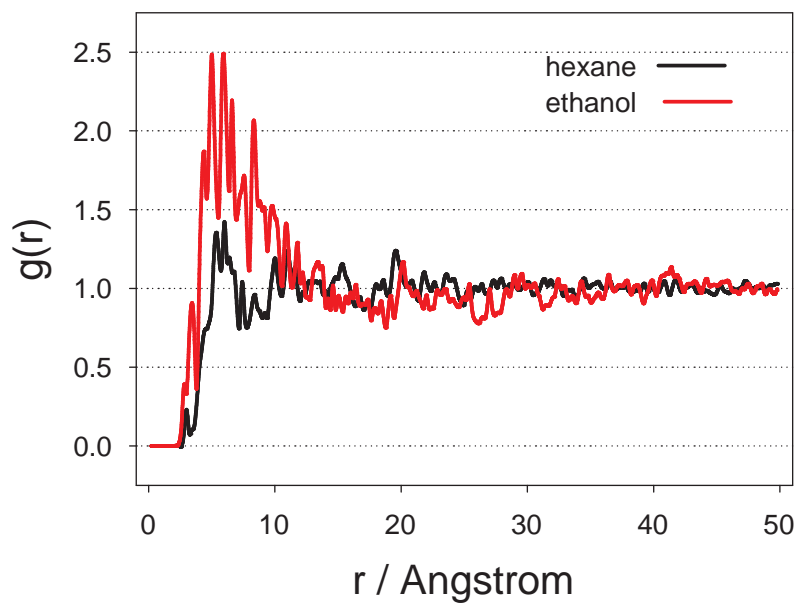
Figure 29: The radial distribution function in each solvent (ethanol and hexane) from the center of mass of solute molecule (CHD); red and black lines obtained by the respective simulations in ethanol and hexane solvents.

5. Future perspectives

The ZN-TSH method was shown to be useful to clarify various nonadiabatic chemical dynamics. The method can be combined with the QM/MM method and with the PME (particle-mesh Ewald) method to investigate nonadiabatic chemical and biological dynamics embedded in environment such as protein environment and solvent. If necessary, various phases including those induced by nonadiabatic transitions can be incorporated. The corresponding method is called ZN-HKSCIVR, in which the Zhu-Nakamura formulas are incorporated into the Herman-Kluk type semiclassical initial value representation method[44]. Although in this review article we have mainly reported the works carried out by the present authors' research groups, some other groups have also employed the Zhu-Nakamura theory to clarify the nonadiabatic chemical dynamics of polyatomic molecules. Examples are nonadiabatic *ab initio* molecular dynamics of photoisomerization in bridged azobenzene by Han's group[189] and in azobenzene by Zhu's group[190].

The various methods explained in this review article present promising approaches with a wide range of chemical and biological applications. Examples of useful future applications would be photochromism[4], molecular switches[5], molecular machines[6], molecular devices[7], photo-synthesis[23], and solar cells[191]. Another interesting field is to clarify the isotopic variations of atmospheric molecules in geologically old age in the field of geochemistry[192]. In all these systems, nonadiabatic transitions are supposed to play crucial roles.

Quantum mechanical tunneling as another important quantum effect can be incorporated into the above scheme[45]. Along classical trajectories one can detect caustics which define the boundary between classically allowed and forbidden regions and an optimal tunneling path can be defined starting from each caustic. By doing this a semiclassical molecular dynamics simulation method can be developed, in which all the important quantum mechanical effects can be taken into account.

Another important application of the above methods is laser control of chemical dynamics[193]. Conical intersections can be created by shining laser, as can be understood from the picture of "dressed state" that means that potential energy surfaces are shifted up and down by the amount of photon energy. The diabatic coupling at this artificially created conical intersection is the laser-molecule dipole interaction and thus by manipulating laser parameters such the frequency, strength and polarization, not only the wave packet motion but also the nonadiabatic transitions at the conical intersections can be controlled in a desirable way. In such a way, not only clarifying the dynamics but also controlling and designing reactions would become possible.

There are some general problems to be overcome in the present methods described above. The first one is the large amount of cpu-time due to time consuming *ab initio* quantum chemical computations. On-the-fly scheme saves time quite a lot compared to the *ab initio* computation of global potential energy surfaces in advance. However, accurate evaluation of conical intersections requires high-level of

quantum chemical computations, which is very much time consuming even in the on-the-fly method. One good solution is to use highly parallelized computers, since each classical trajectory can be run independently. The second one is the dimensionality problem, namely, we have to figure out a good way to reduce the dimension of the central reaction system not only in the nonadiabatic transition case but also in the quantum mechanical tunneling case. The third problem is that we usually don't know in advance where conical intersections or potential barriers (transition states) exist in the high dimensional systems. It would probably be useful to employ a method such as the one proposed by Maeda and Ohno[194] with use of low level of quantum chemical methods before starting real heavy computations.

Acknowledgments

Appendix

Fortran code for the Zhu-Nakamura formulas

The attached routines written in Fortan are used for ZN-TSH computation. The main subroutine for the ZN formulas is "hop.f" at the top of the hierarchy structure shown below. This routine returns the hopping probability between the two potential energy surfaces and the corresponding phase induced by the transition.
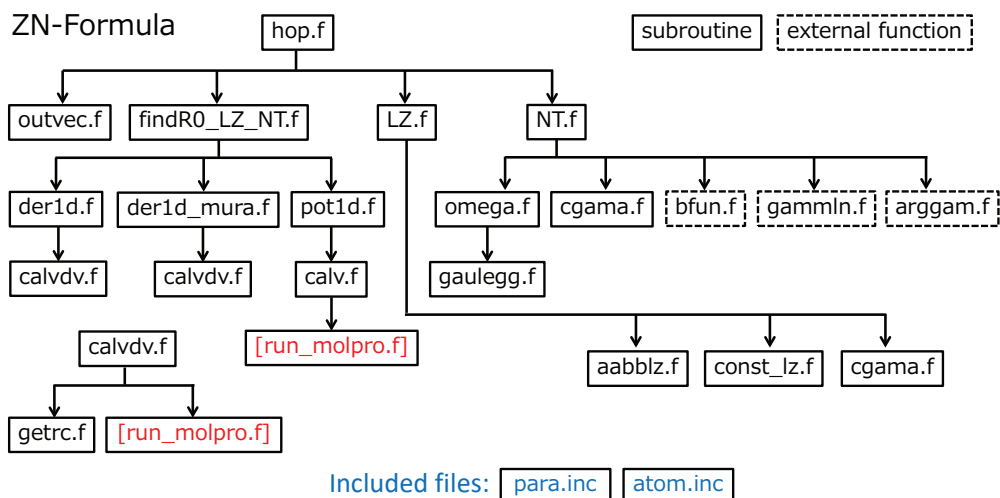

Figure 30: Hierarchy of subroutines to compute nonadiabatic transition probabilities and phases.

Figure 30 shows all the routines and their hierarchy. The "run_molpro.f" in red represents the routine that should be supplied by the user. Here, it is assumed that the Molpro (version 2012)[142] is employed for the on-the-fly *ab initio* computation. Executing "call system("molpro input.com")" in Fortran code, the user can run the *ab initio* program. If the user-supply main program reads the output file and gives all data in the subroutine "hop.f", the code starts to compute the hopping probability. The interfaces of the main subroutine (hop.f) and the user-supply subroutine (run_molpro.f) are shown in the sections **A** and **B** below.

Some of the main subroutines are explained below with the information of the corresponding section and page number in the text.

(i) findR0_LZ_NT.f finds R_0 as shown in Fig.1 in Section 2 on page 6.

(ii) LZ.f computes the quantities in Sections 2.1.1 and 2.2.1 on pages 6-8 and 10-11.

- the transition probability, p_{ZN} [Eqs.(2. 11) and (2. 41)]

- the phases, ψ_{ZN} [Eqs.(2. 15) and (2. 46)], σ_{ZN} [Eqs.(2. 15), (2. 50) and (2. 52)] and
  δ_{ZN} [Eqs.(2. 25), (2. 51) and (2. 53)]

(iii) NT.f computes the quantities in Sections 2.1.2 and 2.2.2 on pages 8-9 and 11-12.

- the transition probability, P_{12} [Eqs.(2. 27), (2. 54) and (2. 59)]
- the phases, $\bar{\phi}_S$ [Eq.(2. 29)], ϕ [Eq.(2. 67)], σ_{ZN} [Eqs.(2. 28), (2. 69) and (2. 62)],
  δ_{ZN} [Eqs.(2. 32), (2. 70) and (2. 61)],
  $\Delta_{12,11,22}$ [Eqs.(2. 36), (2. 37), (2. 38), (2. 64) and (2. 71)] and
  $U_{1,2}$ [Eqs.(2. 40), (2. 35) and (2. 66)]

Note that the main subroutine (hop.f) returns the only hopping probability in the argument of "prob", but the phases listed above are shown on standard output (stdout) in computer (The default destination of stdout is the display screen on computer.). If the phases are required to be stored in arrays, users need to improve the arguments in "hop.f", "LZ.f" and "NT.f."

A. The interface of the main subroutine "hop.f"

> subroutine hop(**etot1d**, **ek1d**, **v1d**, **dir**, **r**, **v**, **ead**, **prob**,
> &   **natom**, **nsurf**, **is0**, **is1**, **keyhop**, **kavail**)

Cartesian coordinates are employed for these arguments; the input/output is indicated in parentheses.

etot1d : energy for hopping direction. (input)

ek1d : kinetic energy for hopping direction. (input)

v1d : velocity in the hopping direction. (input)

dir : hopping direction. (input)

r : current coordinate in atomic unit (a_0). (input)

v : current velocity. (input)

ead : adiabatic potential energies in lower and upper potentials (E_h). (input)

prob : nonadiabatic transition probability. (output)

natom : number of atoms. (input)

nsurf : number of potential energy surfaces taken into account. (input)

is0 : index of the relevant state. (input)

is1 : index of the adjacent state. (input)

keyhop : type for LZ transition ($E \geq E_X$ or $E < E_X$) and NT transition ($E \geq E_b, E_b > E \geq E_t$ or $E < E_t$) by 1-2 and 3-5. (output)

kavail : flag indicating whether the transition is classically allowed or not. If kavail=1, etot1d is not enough to hop vertically. (output)

The sizes of dimension of the arguments are as follows;

- **dir**, **r** and **v** arrays are 3(x$-$, y$-$ and z $-$ components) $\times$ matom; natom $\leq$ matom. (matom is the maximum counting number of atoms defined in the including file, "para.inc.")

- **ead** array is msurf; nsurf $\leq$ msurf. (msurf is the maximum counting number of potential surfaces defined in "para.inc.")

- otherwise, all arrays are single values

B. The interface of the user-supplied subroutine "run_molpro.f"

subroutine run_molpro(**r_c**, **v_c**, **dvdx_c**, **nacme_c**, **tdm_c**,
                            natom, **nsurf**, **isurf1**, **isurf2**, **indgna**)

Cartesian coordinates are employed for the arguments; the input/output is indicated in parentheses. This routine controls the *ab initio* calculation with the argument of "indgna" by 0, 1 and 2.

r_c : current coordinates (a_0). (input)

v_c : adiabatic potential energy (E_h). (output)

dvdx_c : adiabatic potential energy gradient. (output)

nacme_c : nonadiabatic coupling element (nonadiabatic vector). (output)

tdm_c : transition dipole moment. (output)

natom : number of atoms. (input)

nsurf : number of potential energy surfaces taken into account. (input)

isurf1 : index of the relevant state. (input)

isurf2 : index of the adjacent state. (input)

indgna controls the output of energy, gradients, non-adiabatic couplings and so on. (input)

- When indgna = 0, only the potential energy is stored in **v_c**.
- When indgna = 1, potential energy and its gradient are store in **v_c** and **dvdx_c**.
- When indgna = 2, potential energy and nonadiabatic coupling elements are stored in **v_c** and **nacme_c**.

The sizes of dimension for the arguments are as follows;

- **r_c**, **dvdx_c**, **nacme_c** and **tdm_c** arrays are $3 \times$ matom; natom $\leq$ matom. (matom defined in the including file, "para.inc.")

- **v_c** array is msurf; nsurf $\leq$ msurf. (msurf defined in "para.inc.")

- otherwise, all arrays are single values

C. The ZN formulas software archived in Supplemental Information

The software is archived in "http://pweb.cc.sophia.ac.jp/nanbu_lab/zntsh" with zip-format, "src.zip." The archived file includes all files listed in Fig.30. The user should modify the "para.inc" and "atom.inc" depending on the molecular system.

References

[1] W. Domcke, D.R. Yarkony, and H. Koppel, *Conical Intersections, Theory, Computation and Experiment*, (World Scientific, Singapore, 2011).

[2] H. Nakamura, *Nonadiabatic Transition: Concepts, Basic Theories and Applications* (World Scientific, Singapore, 2012).

[3] S. Nanbu, T. Ishida and H. Nakamura, *Chem. Science* **1**, 663 (2010).

[4] *Photochromism: Molecules and Systems* ed. by H. Dürr and H. Bouas-Laurent (Elsevier, Amsterdam, 2003).

[5] *Molecular Switches* ed. by B. Feringa (Wiley-VCH, Weinheim, 2001).

[6] *Molecular Machines and Motors (Structure and Bonding)* ed. by J.P. Sauvage (Springer, Berlin, 2001).

[7] V. Balzani, M. Venturi and A. Credi, *Molecular Devices and Machines: A Journey into the Nanoworld* (Wiley-VCH, Weinheim, 2003).

[8] A. Thiel, *J. PPhys.* **G16**, 867 (1990).

[9] B. Imanishi and W. von Oertzen, *Phys. Rep.* **155**, 29 (1987).

[10] A. Yoshimori and M. Tsukada (ed.), *Dynamical Processes and Ordering on Solid Surfaces* (Springer, Berlin, 1985).

[11] R. Engleman, *Non-Radiative Decay of Ions and Molecules in Solids* (North-Holland, Amsterdam, 1979).

[12] G. Blatter and D.A. Browne, *Phys. Rev.* **B37**, 3856 (1988).

[13] E. Ben-Jacob and Y. Gefen, *Phys. Lett.* **108A**, 289 (1985).

[14] Y. Gefen, E. Ben-Jacob and A.O. Caldeira, *Phys. Rev.* **B36**, 2770 (1987).

[15] J.Q. You and F. Nori, *Physics Today* **58**, 42 (2005).

[16] S.N. Shevchenko, S. Ashhab and F. Nori, *Phys. Rep.* **492**, 1 (2010).

[17] R. Long, N.J. English and O.V. Prezhdo, *J. Phys. Chem. Lett.* **5**, 2941 (2014).

[18] H. Zhu, Y. Yang, K. Hyeon-Deuk, M. Califano, N. Song, Y. Wang, W. Zhang, O.V. Prezhdo and T. Lian, *Nano Lett.* **14**, 1263 (2014).

[19] J. Liu and O.V. Prezhdo, *J. Phys. Chem. Lett.* **6**, 4463 (2015).

[20] B. Schwarzschild, *Physics Today* **June 17**, (1986).

[21] B. Schwarzschild and M.H. Pinsonneault, *Rev. Mod. Phys.* **64**, 885 (1992).

[22] D.W. Lawlor, *Photosynthesis* (Springer, New York, 2001).

[23] R.E. Blankenship, *Molecular Mechanisms of Photosynthesis* (Blackwell Science, Oxford, 2002).

[24] T.P. Sakmar, S.T. Menon, E.P. Marin and E.S. Awad, *Annu. Rev. Biophys. Biomol. Structure* **31**, 443 (2002).

[25] M. Chalfie and S.R. Kain, *Green Fluorescent Proteins, Properties, Applications, and Protocols* (John Wiley and Sons, Hoboken, 2006).

[26] E.E. Nikitin and S.Ya. Umanskii, *Theory of Slow Atomic Collisions* (Springer, Berlin, 1984).

[27] M.S. Child, *Semiclassical Mechanics with Molecular Applications* (Clarendon, Oxford, 1991).

[28] E.S. Medvedev and V.I. Osherov, *Radiationless Transitions in Polyatomic Molecules, Springer Series in Chemical Physics*, **57** (Springer, Berlin, 1994).

[29] W.H. Miller, *J. Phys. Chem.* **A113**, 1405 (2009).

[30] L.D. Landau, *Phys. Zts. Sov.* **2**, 46 (1932).

[31] C. Zener, *Proc. Roy. Soc.* **A137**, 696 (1932).

[32] E.C.G. Stückelberg, *Hel. Phys. Acta.* **5**, 369 (1932).

[33] (a) C. Zhu and H. Nakamura, *J. Chem. Phys.* **97**, 8497 (1992); (b) ibid, **98**, 6208 (1993); (c) ibid, **101**, 4855 (1994); (d) ibid, **101**, 10630 (1994); (e) ibid, **102**, 7448 (1995); (f) ibid, **106**, 2599 (1997); (g) ibid, **107**, 7839 (1997); (h) ibid, **108**, 7501 (1998); (i) ibid, **109**, 4689 (1998); (j) *Chem. Phys. Lett.* **258**, 342 (1996); (k) ibid, **274**, 205 (1997); (l) H. Nakamura, *XXI-ICPEAC Invited Talks* (Amer. Inst. Phys., Woodbury, New York, 2000) p.495; (m) H. Nakamura, *Adv. Chem. Phys.* **82**, 243 (1992); (n) ibid, **138**, 95 (2008); (o) C. Zhu, Y. Teranishi and H. Nakamura, *Adv. Chem. Phys.* **117**, 127 (2001).

[34] *Multidimensional Quantum Dynamics: MCTDH Theory and Applications*, ed. by H-D Meyer, F. Gatti and G.A. Worth (Wiley-VCH, Berlin, 2009).

[35] A. Bjerre and E.E. Nikitin, *Chem. Phys. Lett.* **1**, 179 (1967).

[36] J.C. Tully and R. Preston, *J. Chem. Phys.* **54**, 4297 (1970).

[37] J.C. Tully, *J. Chem. Phys.* **93**, 1061 (1990).

[38] J.C. Tully, *J. Chem. Phys.* **137**, 22A301 (2012).

[39] T. Nelson, S. Fernandez-Alberti, A.E. Roitberg and S. Tretiak, *Accounts of Chemical Research* **47**, 1155 (2014).

[40] I. Tavernelli, *Accounts of Chemical Research*, **48**, 792 (2014).

[41] L. Wang, A. Akimov and O.V. Prezhdo, *J. Phys. Chem. Lett.* **7**, 2100 (2016).

[42] W.H. Miller, *Adv. Chem. Phys.* **101**, 853 (1997); W.H. Miller, *J. Phys. Chem.* **A105**, 2942 (2001); K.G. Kay, *Annu. Rev. Phys. Chem.* **56**, 255 (2005).

[43] E.J. Heller, *J. Chem. Phys.* **75**, 2923 (1981).

[44] M.F. Herman, *Annu. Rev. Phys. Chem.* **45**, 83 (1994).

[45] H. Nakamura, S. Nanbu, Y. Teranishi and A. Ohta, *Phys. Chem. Chem. Phys.* **18**, 11972 (2016).

[46] P.S. Julienne and M.J. Krauss, *J. Mol. Spectr.* **56**, 270 (1975).

[47] J.C. Tully and R.K. Preston, *J. Chem. Phys.* **81**, 4352 (1971).

[48] P. Oloyede, G.V. Mil'nikov and H. Nakamura, *J. Chem. Phys.* **124**, 144110 (2006).

[49] For instance, D.R. Yarkony, *Rev. Mod. Phys.* **68**, 985 (1996).

[50] E.J. Heller, *J. Chem. Phys.* **68**, 2066, 3891 (1978).

[51] A. Kondorskii and H. Nakamura, *J. Chem. Phys.* **120**, 8937 (2004).

[52] E.J. Heller and R.C. Brown, *J.Chem. Phys*, **79**, 3336 (1983).

[53] J.C. Lorquet and B. Leyh-Nihant, *J. Phys. Chem.* **92**, 4778 (1988).

[54] A.J. Marks and D.L. Thompson, *J. Chem. Phys.* **96**, 1911 (1992).

[55] Y. Okuno and S. Mashiko, *Int. J. Quant. Chem.* **102**, 8 (2005).

[56] J.N. Harvey, *Phys. Chem. Chem. Phys.* **9**, 331 (2007).

[57] R.A. Marcus and N. Sutin, *Biochim. Biophys. Acta* **811**, 265 (1985).

[58] M. Bixon and J. Jortner, *Adv. Chem. Phys.* **106**, 35 (1999).

[59] A.V.Z. Brazykin, P.A. Frantsuzov, K. Seki and M. Tachiya, *Adv. Chem. Phys.* **123**, 511 (2002).

[60] (a) Y. Zhao, G. Mil'nikov and H. Nakamura, *J. Chem. Phys.* **121**, 8854 (2004); (b) Y.Zhao, W. Liang and H. Nakamura, *J. Phys. Chem.* **A110**, 8204 (2006); (c) Y. Zhao and H. Nakamura, *J. Theor. Comp. Chem.* **5**, 299 (2006); (d) Y. Zhao, X. Li, Z. Zhen and W.Z. Liang, *J. Chem. Phys.* **124**, 114508 (2006); (e) Y. Zhao, M.M. Han, W.Z. Liang and H. Nakamura, *J. Phys. Chem.* **A111**, 2047 (2007).

[61] Y. Teranishi, H. Nakamura and S.H. Lin, *AIP Conf. Proc., Theory and Applications in Computational Chemistry: The First Decade of the second Millennium* **1456**, 119 (2012).

[62] S. Miertu, E. Scrocco, J. Tomasi, *Chem. Phys.*, **55**, 117 (1981).

[63] B. Mennucci, *WIREs Comput. Mol. Sci.*, **2**, 386 (2012).

[64] J. Tomasi, B. Mennucci, R. Cammi, *Chem. Rev.*, **105**, 2999 (2005).

[65] L. J. Lowden and D. Chandler, *J. Chem. Phys.*, **59**, 6587 (1973).

[66] L. J. Lowden and D. Chandler, *J. Chem. Phys.*, **61**, 5228 (1974).

[67] S. Ten-no, F. Hirata, S. Kato, *Chem. Phys. Lett.*, **214**, 391 (1993).

[68] M. Kawata, S. Tenno, S. Kato, F. Hirata, *Chem Phys. Lett.*, **240**, 199 (1995).

[69] M. Kawata, S. Tenno, S. Kato, F. Hirata *Chem Phys.*, **203**, 53 (1996).

[70] T. Miyata and F. Hirata, *J. Comput. Chem.*, **29**, 871 (2008).

[71] D. A. Case et al., AMBER9 University of California, San Francisco (2006).

[72] J. Wang, W. Wang, P. A. Kollman, D. A. Case, *J. Mol. Graph. Model.*, **25**, 247 (2006).

[73] J. Wang, R. M. Wolf, J. W. Caldwell, P. A. Kollman, D. A. Case, *J. Comput. Chem.*, **25**, 1157 (2004).

[74] L. Verlet, *Phys. Rev.*, **159**, 98 (1967).

[75] M. P. Allen and D. J. Tildesley, *Computer Simulation in Chemical Physics*, Kluwer Academic Publishers (1992, p.34).

[76] T. Darden, D. York, L. G. Pedersen, *J. Chem. Phys.*, **98**, 10089 (1993).

[77] U. Essmann, L. Perera, M. L. Berkowitz, T. Darden, H. Lee, L. G. Pedersen, *J. Chem. Phys.*, **103**, 8577 (1995).

[78] L.W. Chung, X. Li, H. Hirao, K. Morokuma, *WIREs Comput. Mol. Sci.*, **00**, 1 (2011).

[79] T. Vreven, K.S. Byun, I. Komaromi, S. Dapprich, J.A. Montgomery, K. Morokuma, M.J. Frisch, *J. Chem. Theory Comput.*, **2**, 815, (2006).

[80] A. Heyden, H. Lin, D.G. Truhlar, *J. Phys. Chem. B*, **111**, 2231 (2007).

[81] X. Li, L. W. Chung, H. Mizuno, A. Miyawaki, K. Morokuma, *J. Phys. Chem. B*, **114**, 1114 (2010).

[82] T. Kerdcharoen and K. Morokuma, *J. Chem. Phys.*, **118**, 8856 (2003).

[83] N. Takenaka, Y. Kitamura, Y. Koyano, M. Nagaoka, *Chem. Phys. Lett.*, **524**, 56 (2012).

[84] P. Sripa, A. Tongraar, T. Kerdcharoen, *J. Phys. Chem. A*, **117**, 1826 (2013).

[85] R.S. Becker, K. Freedman, J.A. Hutchinson, L. J. Noe, *J. Am. Chem. Soc.*, **107**, 3942 (1985).

[86] D. Huppertt, P.M. Rentzepis, *J. Phys. Chem.*, **90**, 2813 (1986).

[87] H. Kandori, Y. Katsuta, M. Ito, H. Sasabe, *J. Am. Chem. Soc.*, **117**, 2669 (1995).

[88] R.S. Becker and K. Freedman, *J. Am. Chem. Soc.*, **107**, 1477 (1985).

[89] R. Mathies and C. Brito, *Science*, **240**, 777 (1988).

[90] K.A. Freedman and R.S. Becker, *J. Am. Chem. Soc.*, **108**, 1245 (1986).

[91] J. Tittor and D. Oesterhelt, *FEBS Lett.*, **263**, 269 (1990).

[92] H. Kandori and H. Sasabe, *Chem. Phys. Lett.*, **216**, 126 (1993).

[93] P. Hamm, M. Zurek, T. Röschinger, H. Patzelt, D. Oesterhelt, W. Zinth, *Chem. Phys. Lett.*, **263**, 613 (1996).

[94] G. Zgrabli, K. Voïtchovsky, M. Kindermann, S. Haacke, M. Chergui, *Biophys. J.*, **88**, 2779 (2005).

[95] K. Nam, J. Gao, D. M. York, *J. Chem. Theo. Comput.*, **1**, 2 (2005).

[96] O. Kobayashi and S. Nanbu, *Chem. Phys.* **461**, 47 (2015).

[97] O. Kobayashi, "Theoretical studies of molecular electron dynamics on atto- to picosecond time scale", *Doctoral Thesis*, Chaps. 2 and 3, Sophia Univ. (2016).

[98] V.G. Ushakov, K. Nobusada and V.I. Osherov, *Phys. Chem. Chem. Phys.* **3**, 63 (2001).

[99] C. Zhu, H. Kamisaka and H. Nakamura, *J. Chem. Phys.* **116**, 3234 (2002).

[100] B. Li and Ke-Li Han, *J. Chem. Phys.* **128**, 114116 (2008).

[101] T. Murakami, "Nonadiabatic *ab initio* semiclassical molecular dynamics on the multidimensional photochemical reactions", *Doctoral Thesis*, Chap. 5, Sophia Univ. (2015).

[102] V. Vaida, M.I. McCarthy, P. C. Engelking, P. Rosmus, H. J. Werner, P. Botschwina, *J. Chem. Phys.*, **86**, 6669 (1987).

[103] A. Nakajima, K. Fuke, K. Tsukamoto, Y. Yoshida, K. Kaya, *J. Phys. Chem.*, **95**, 571 (1991).

[104] X. Zhu, J -Y. Ma, D. R. Yarkony, H. Guo, *J. Chem. Phys.*, **136**, 234301 (2012).

[105] M. Toplar and N. Makri, *J. Phys. Chem.* **100**, 4330 (1996).

[106] S.F. Nelsen, M.N. Weaver, A.E. Konradsson, J.P. Telo and T. Clark, *J. Amer. Chem. Soc.* **126**, 15431 (2004).

[107] G. Nan, L. Wang, X. Yang, Z. Shuai and Y. Zhao, *J. Chem. Phys.* **130**, 024704 (2009).

[108] Y. Zhao and W.Z. Liang, *Chem. Soc. Rev.* **41**, 1075 (2012).

[109] S.F. Nelsen, A.E. Konradsson, M.N. Weaver, R.M. Stephenson, J.V. Lockard, J.I. Zink and Y. Zhao, *J. Phys. Chem.* **B111**, 6776 (2007).

[110] J. Farquhar, H. Bao, M. Thiemens, *Science*, **289**, 756 (2000).

[111] J. F. Kasting, *Science*, **293**, 819 (2001).

[112] Y. Ueno, M. S. Johnson, S. O. Danielache, C. Eskebjerg, A. Pandey, N. Yoshida, *Proc. Natl. Acad. Sci. U. S. A.*, **106**, 14784 (2009).

[113] J. Savarino, A. Romero, J. Cole-Dai, S. Bekki, M.H. Thiemens, *Geophys. Res. Lett.*, **30** 2131 (2003).

[114] S. Hattori, J.A. Schmidt, M.S. Johnson, S.O. Danielache, A. Yamada, Y. Ueno, N. Yoshida, *Proc. Natl. Acad. Sci. U. S. A.*, **110**, 17656 (2013).

[115] S. Chakraborty, T.L. Jackson, M. Ahmed, M.H. Thiemens, *Proc. Natl. Acad. Sci. U. S. A.* **110**, 17650 (2013).

[116] H.B. Franz, S.-T. Kim, J. Farquhar, J.M.D. Day, R.C. Economos, K.D. McKeegan, A.K. Schmitt, A.J. Irving, J. Hoek, J. Dottin III, *Nature*, **508**, 364 (2014).

[117] A.R. Whitehill, C. Xie, X. Hu, D. Xie, H. Guo, S. Ono, *Proc. Natl. Acad. Sci. U. S. A.*, **110**, 17697 (2013).

[118] S.O. Danielache, S. Tomoya, A. Kondorsky, I. Tokue, S. Nanbu, *J. Chem. Phys.*, **140**, 044319 (2014).

[119] Murakami, A. Ohta, T. Suzuki, K. Ikeda, S.O. Danielache, S. Nanbu, *Chem. Phys.*, **452**, 17 (2015).

[120] P.N. Prasad, *Introduction to Biophotonics* (John Wiley & Sons, 2003).

[121] L.O. Björn, *The Photochemical Reactions in Biological Light Perception and Regulation* In *Photobiology: The Science Light and Life* ed. L.O. Björn (Kluwer Academic, Dordrecht, 2002), p.157.

[122] T. Ishida, S. Nanbu and H. Nakamura, *J. Phys. Chem.* **A113**, 4356 (2009).

[123] D. Marx and J. Hutter, *Ab initio MD: Theory and Imprementation*, in *Modern Methods and Algorithms of Quantum Chemistry*, ed. J. Grotendorst, John von Neumann Institute for Computing, NIC series, 2000, vol.1.

[124] H.-J. Werner and P.J. Knowles, *J. Chem. Phys.* **82**, 5053 (1985).

[125] M.J. Frisch *et al.*, Gaussian03, Revision D.01, Gaussian Inc. (Wallingfold, CT, 2004).

[126] W.C. Chung, S. Nanbu and T. Ishida, *J. Phys. Chem.* **A114**, 8190 (2010).

[127] H. Nakamichi, V. Buss and T. Okada, *Biophys. J* **92**, L106 (2007).

[128] J.B. Hurley, T.G. Ebrey, B. Honig and M. Ottolenghi, *Nature* **270**, 540 (1977).

[129] T. Okada, M. Sugihara, A.N. Bondar, M. Elstner, P. Entel and V. Buss, *J. Mol. Biol.* **342**, 571 (2004).

[130] S. Sekharan, M. Sugihara, O. Weingart, T. Okada and V. Buss, *J. Am. Chem. Soc.* **129**, 1052 (2007).

[131] T. Murakami, M. Nakazono, A. Kondorskiy, T. Ishida, S. Nanbu, *Phys. Chem. Chem. Phys.*, **14**, 11546 (2012).

[132] H.-J. Werner *et al.*, MOLPRO Version 2008.1; A Package of *ab initio* Programs, Cardiff University, Cardiff, UK, 2008.

[133] (a) R.W. Schoenlein, L.A. Peteanu, R.A. Mathies and C.V. Shank, *Science* **254**, 412 (1991); (b) L.A. Peteanu, R.W. Schoenlei, Q. Wang, R.A. Mathies and C.V. Shank, *Proc. Natl. Acad. Sci. U.S.A.* **90**, 11762 (1993); (c) R.W. Schoenlei, L.A. Peteanu, Q. Wang, R.A. Mathies and C.V. Shank, *J. Phys. Chem.* **97**, 12087 (1993).

[134] H.J. Dartnall, C.F. Goodeve and R.V. Lythgoe, *Proc. Roy. Soc.*, **A156**, 158 (1936).

[135] J.E. Kim, M.J. Tauber and R.A. Mathies, *Biochemistry* **40**, 13774 (2001).

[136] W.C. Chung, S. Nanbu and T. Ishida, *J. Phys. Chem.* **B116**, 8009 (2012); *ibid Chem. Lett.* **40**, 1395 (2011).

[137] W.D. Cornell, P. Cieplak, C.I. Bayly, I.R. Gould, K.M. Merz, D.M. Ferguson, D.C. Spellmeyer, T. Fox, J.W. Caldwell and P.A. Kollman, *J. Am. Chem. Soc.* **117**, 5179 (1995).

[138] H.R. May, In *Dynamics of Molecules and Chemical Reactions* ed. R.E. Wyatt and J.Z.H. Zhang (Marcel Dekker, Inc., New York, 1996), p.589.

[139] H. Nakamichi and T. Okada, *Angew. Chem. Int. Ed.* **45**, 4270 (2006).

[140] M. J. Frisch *et al.*, Gaussian 09, Revision C.01, Gaussian, Inc., Pittsburgh, PA, (2009).

[141] Y. Sakai, H. Tatewaki and S. Huzinaga, *J. Comp. Chem.* **2**, 108 (1981).

[142] H.-J. Werner *et al.*, MOLPRO Version 2012.1; A Package of *ab initio* Programs, Cardiff University, Cardiff, UK, 2012.

[143] T. Mori, K. Nakano, S. Kato, *J. Chem. Phys.* **133**, 064107 (2010).

[144] S.L. Logunov, L. Song and M.A. El-Sayed, *J. Phys. Chem.* **100**, 18586 (1996).

[145] M. Irie, *Chem. Rev.*, **100**, 1685 (2000).

[146] M. Irie, S. Kobatake, M. Horichi, *Science*, **291**, 1769 (2001).

[147] M. Murakami, H. Miyasaka, T. Okada, S. Kobatake, M. Irie, *J. Am. Chem. Soc.*, **126**, 14764 (2004).

[148] K.L. Kompa, R.D. Levine, *Proc. Natl. Acad. Sci. U. S. A.*, **98**, 410 (2001). S. Mahvidi, S. Takeuchi, S. Kusumoto, H. Sato, T. Nakagawa, Y. Yokoyama, *Org. Lett.*, **18**, 5042 (2016).

[149] P. Celani, S. Ottani, M. Olivucci, F. Bernardi, M.A. Robb, *J. Am. Chem. Soc.*, **116**, 10141 (1994).

[150] P. Celani, F. Bernardi, M.A. Robb, M. Olivucci, *J. Phys. Chem.*, **100**, 19364 (1996).

[151] M. Garavelli, P. Celani, M. Fato, M.J. Bearpark, B.R. Smith, M. Olivucci, M.A. Robb, *J. Phys. Chem. A*, **101**, 2023 (1997).

[152] M. Garavelli, P. Celani, F. Bernardi, M.A. Robb, M. Olivucci, *J. Am. Chem. Soc.*, **119**, 11487 (1997).

[153] M. Garavelli, F. Bernardi, M. Olivucci, T. Vreven, S. Klein, P. Celani, M.A. Robb, *Faraday Discuss.*, **110**, 51 (1998).

[154] M. Garavelli, C.S. Page, P. Celani, M. Olivucci, W.E. Schmid, S.A. Trushin, W. Fuß, *J. Phys. Chem. A*, **105**, 4458 (2001).

[155] A. Hofmann, R. de Vivie-Riedle, *J. Chem. Phys.*, **112**, 5054 (2000).

[156] A. Hofmann, R. de Vivie-Riedle, *Chem. Phys. Lett.*, **346** 299 (2001).

[157] L. Kurtz, A. Hofmann, R. de Vivie-Riedle, *J. Chem. Phys.*, **114**, 6151 (2001).

[158] A. Hofmann, L. Kurtz, R. de Vivie-Riedle, *Appl. Phys. B*, **71**, 391 (2000).

[159] H. Tamura, S. Nanbu, H. Nakamura, T. Ishida, *Chem. Phys. Lett.*, **401**, 487 (2005).

[160] H. Tamura, S. Nanbu, T. Ishida, H. Nakamura, *J. Chem. Phys.*, **124**, 084313 (2006).

[161] C. Nonnenberg, S. Grimm, I. Frank, *J. Chem. Phys.*, **119**, 11585 (2003).

[162] M. Boggio-Pasqua, M. Ravaglia, M. J. Bearpark, M. Garavelli, M.A. Robb, *J. Phys. Chem. A*, **107**, 11139 (2003).

[163] J.B. Schönborn, J. Sielk, B. Hartke, *J. Phys. Chem. A*, **114**, 4036 (2010).

[164] A. Ohta, "Theoretical study of chemical dynamics for condensed phase", *Doctoral Thesis*, Chaps. 2 and 3, Sophia Univ. (2017).

[165] A. Ohta, O. Kobayashi, S.O. Danielache, S. Nanbu, *Chem. Phys.*, **459**, 45 (2015).

[166] A. Ohta, O. Kobayashi, S.O. Danielache, S. Nanbu, *Chem. Phys.*, **485**, 45 (2017).

[167] M.O. Trulson, G.D. Dollinger, R.A. Mathies, *J. Am. Chem. Soc.*, **109**, 586 (1987).

[168] M.O. Trulson, G.D. Dollinger, R.A. Mathies, *J. Chem. Phys.*, **90**, 4274 (1989).

[169] P.J. Reid, S.J. Doig, R.A. Mathies, *Chem. Phys. Lett.*, **156**, 163 (1989).

[170] P.J. Reid, S.D. Wickham, R.A. Mathies, *J.Phys.Chem.*, **96**, 5720 (1992).

[171] P.J. Reid, S.J. Doig, S.D. Wickham, R.A Mathies, *J. Am. Chem. Soc.*, **115**, 4754 (1993).

[172] M.K. Lawless, S.D. Wickham, R.A. Mathies, *Acc. Chem. Res.*, **28**, 493 (1995).

[173] S.H. Pullen, L.A. Walker II, B. Donovan, R.J. Sension, *Chem. Phys. Lett.*, **242**, 415 (1995).

[174] S.H. Pullen, N.A. Anderson, L.A. Walker II, R.J. Sension, *J. Chem. Phys.*, **107**, 4985 (1997).

[175] S.H. Pullen, N.A. Anderson, L.A. Walker II, R.J. Sension, *J. Chem. Phys.*, **108**, 556 (1998).

[176] S. Lochbrunner, W. Fuß, W.E. Schmid, K. L.Kompa, *J. Phys. Chem. A*, **102**, 9333 (1998).

[177] W. Fuß, T. Schikarski, W.E. Schmid, S. Trushin, K.L. Kompa, *Chem. Phys. Lett.*, **262**, 675(1996).

[178] S.A. Trushin, W. Fuß, T. Schikarski, W.E. Schmid, K.L. Kompa, *J. Chem. Phys.*, **106**, 9386 (1997).

[179] W. Fuß, W.E. Schmid, S.A. Trushin, *J. Chem. Phys.*, **112**, 8347 (2000).

[180] N. Kuthirummal, F.M. Rudakov, C.L. Evans, P.M. Weber, *J. Chem. Phys.*, **125**, 133307 (2006).

[181] R.C. Dudek, P.M. Weber, *J. Phys. Chem. A*, **105**, 4167 (2001).

[182] J.D. Cardoza, R.C. Dudek, R.J. Mawhorter, P.M. Weber, *Chem. Phys.*, **299**, 307 (2004).

[183] C.Y. Ruan, V.A. Lobastov, R. Srinivasan, B.M. Goodson, H. Ihee, A.H. Zewail, *Proc. Natl. Acad. Sci. U. S. A.*, **98**, 7117 (2001).

[184] H. Ihee, V.A. Lobastov, U.M. Gomez, B.M. Goodson, R. Srinivasan, C.Y. Ruan, A.H. Zewail, *Science*, **291**, 458 (2001).

[185] K. Kosma, S.A. Trushin, W. Fuß, W.E. Schmid, *Phys. Chem. Chem. Phys.*, **11**, 172 (2009).

[186] S. Adachi, M. Sato, T. Suzuki, *J. Phys. Chem. Lett.*, **6**, 343 (2015).

[187] M.P. Minitti, J.M. Budarz, A. Kirrander, J.S. Robinson, D. Ratner, T.J. Lane, D. Zhu, J.M. Glownia, M. Kozina, H.T. Lemke, M. Sikorski, Y. Feng, S. Nelson, K. Saita, B. Stankus, T. Northey, J.B. Hastings, P.M. Weber, *Phys. Rev. Lett.*, **114**, 255501 (2015).

[188] A.M.A. Dias, R.P. Bonifácio, I.M. Marrucho, A.A.H. Pádua, M.F. Costa Gomes, *Phys. Chem. Chem. Phys.*, **5**, 543 (2003).

[189] A.H. Gao, B. Li, P.Y. Zhang and K.L. Han, *J. Chem. Phys.* **137**, 204305 (2012).

[190] L. Yu, C. Xu and C. Zhu, *Phys. Chem. Chem. Phys.* **17**, 17646 (2015).

[191] *Organic Solar Cells: Materials, Devices, Interfaces, and Modeling* ed. Q. Qiao (CRC Press, Boca Raton, 2015).

[192] J.A. Schmidt, M.S. Johnson, S. Hattori, N. Yoshida, S. Nanbu and R. Schinke, *Atmos. Chem. and Phys.* **13**, 1511 (2013).

[193] A. Kondorskiy, S. Nanbu, Y. Teranishi and H. Nakamura, ɟ. Phys. Chem. **A114**, 6171 (2010).

[194] S. Maeda, K. Ohno and K. Morokuma, *J. Phys. Chem.* **A113**, 1704 (2009); ibid, *J. Chem. Theory Comput.* **6**, 1538 (2010).